Analytic Kerr black hole lensing for equatorial observers in the strong deflection limit

V. Bozza,[1,2,3] F. De Luca,[2,3,4] G. Scarpetta,[2,3,5] and M. Sereno[3,6,7]

[1]*Centro Studi e Ricerche "Enrico Fermi," Compendio Viminale, I-00184, Rome, Italy*
[2]*Dipartimento di Fisica "E. R. Caianiello," Università di Salerno, via Allende, I-84081 Baronissi (SA), Italy*
[3]*Istituto Nazionale di Fisica Nucleare, Sezione di Napoli, Italy*
[4]*Institut für Theoretische Physik der Universität Zürich, CH-8057 Zürich, Switzerland*
[5]*International Institute for Advanced Scientific Studies, Vietri sul Mare (SA), Italy*
[6]*Dipartimento di Scienze Fisiche, Università degli Studi di Napoli 'Federico II', Via Cinthia, Monte S. Angelo, 80126 Napoli, Italy*
[7]*Istituto Nazionale di Astrofisica, Osservatorio Astronomico di Capodimonte, Salita Moiariello, 16, 80131 Napoli, Italy*

(Received 29 July 2005; published 19 October 2005)

In this paper we present an analytical treatment of gravitational lensing by Kerr black holes in the limit of very large deflection angles, restricting to observers in the equatorial plane. We accomplish our objective starting from the Schwarzschild black hole and adding corrections up to second order in the black hole spin. This is sufficient to provide a full description of all caustics and the inversion of lens mapping for sources near them. On the basis of these formulae we argue that relativistic images of low mass x-ray binaries around Sgr A* are very likely to be seen by future x-ray interferometry missions.

DOI: 10.1103/PhysRevD.72.083003 PACS numbers: 95.30.Sf, 04.70.Bw, 98.62.Sb

I. INTRODUCTION

General relativity predicts that light rays passing close to a black hole suffer gravitational lensing, so that an observer almost aligned with the line connecting a source and a black hole sees two images of the original source. These images are due to small deviations of photons that pass far enough from the black hole to allow a weak field approximation of the metric tensor. However, already Darwin in 1959 noticed that photons passing very close to a black hole may suffer much larger deflections without falling into the event horizon [1]. In principle, an observer situated on the line connecting the source and the black hole, besides the two classical weak field images, would detect two infinite series of images very close the black hole. These images are produced by photons making one or more complete loops around the black hole before reemerging in the observer direction. Of course, these relativistic images are largely demagnified with regard to (w.r.t.) the original source and for some time they just remained a mathematical curiosity of general relativity.

Nevertheless, things changed after the great progress of interferometric techniques and the widely accepted opinion that the radio-source Sgr A* in the Galactic center actually hosts a supermassive black hole of 3.61×10^5 solar masses [2] (for a review see [3]). These facts motivated Virbhadra and Ellis to propose that this black hole may be an ideal candidate for the generation of relativistic images of sources eventually passing behind it [4]. In fact, the angular radius of the shadow of Sgr A* is predicted to be 23 μas, which is comparable to the best resolution achieved in the millimeter band (18 μas [5]). A complete imaging in the sub-mm band was suggested in Ref. [6]. Future space missions in the infrared and in the x rays may reach even higher resolutions (for a complete discussion, see Ref. [7]).

A new field of Gravitational lensing was definitively opened and several authors proposed alternative methods to overcome the evident difficulties of full general relativity calculations of geodesics which typically result in cumbersome equations and heavy numerical integrations [8,9]. However, Darwin himself proposed a surprisingly easy formula for the positions of the relativistic images generated by a Schwarzschild black hole [1]. This formula and its consequences were later discussed or rediscovered several times [10–13] before the Virbhadra and Ellis proposal. After that work, it was revived in Ref. [14], where it was called the strong field limit of the deflection angle. It was then extended to Reissner-Nordstrom black holes in Ref. [15] and applied to microlensing by Sgr A* by Petters [16]. In this paper, as suggested by Perlick [9], we shall revise this terminology, referring to a strong deflection limit (SDL), since an infinite deflection angle is not necessarily related to a large curvature. This can be realized by considering a very large black hole. The minimum distance reachable by a photon without being captured is of the same order of the horizon radius. The Riemann invariant $R_{\alpha\beta\gamma\delta}R^{\alpha\beta\gamma\delta}$, evaluated in the inner region probed by the photon, scales as the curvature at the horizon, i.e. $1/M^4$. Increasing the mass of the black hole, the curvature felt by the photon becomes arbitrarily low, even if its deflection may be large. So, it is more correct to speak of a strong deflection limit without referring to the curvature.

The power of the SDL expansion of the deflection angle became evident when its universality was demonstrated in Ref. [17]. Any class of spherically symmetric black holes leads to the same SDL expansion; the coefficients of this expansion depend on the specific class of the black hole, representing a sort of identity card, from which all the parameters of the black hole can be extracted. By observing the relativistic images of a gravitational lensing event induced by a black hole, it is possible, in principle, to

deduce all its parameters and properties. Since this could also provide the key to discriminate between general relativity and some extended theories of gravitation, this method has been applied to several interesting classes of black holes coming from string theory, braneworlds, and wormholes [18]. Some limitations were removed in Refs. [19,20], while time delay analysis was performed in Ref. [21].

As regards spinning black holes, the story is more complicated. Almost 40 years have passed since Carter reduced the geodesics equations in Kerr spacetime to first order equations depending on four constants of motion [22]. This fundamental achievement allowed a complete study and classification of all possible trajectories of massive particles and photons moving around spinning black holes [23]. In order to visualize and study these geodesics, a very large amount of numerical methods has been developed through years. In the context of gravitational lensing, these methods have been used to describe the light curve of a star orbiting a black hole [24] and the apparent shape of the accretion disk [11,25]. Rauch and Blandford have proved the formation of extended 4-cusped caustics numerically [26].

Extending the SDL methodology to axially symmetric black holes is not immediate and the simplicity of the approach may be easily lost. In Ref. [27] the SDL formula was recovered for light rays lying close to the equatorial plane of a Kerr black hole, but the coefficients of the formula had to be calculated numerically as functions of the black hole spin. Vazquez and Esteban solved the lens equation far from the equatorial plane for some particular cases [28], but a complete analytical treatment of Kerr lensing is still missing.

In this paper we make a considerable step toward this objective, focusing on observers lying on the equatorial plane and solving the general lens equation for small values of the black hole spin. Perturbative methods allow us to use the Schwarzschild SDL formula as starting point to describe the deflection of light rays looping around a Kerr black hole in a completely analytical way. Our treatment leads to an amazingly simple description of all relativistic caustics and to the immediate inversion of lens mapping for sources near caustics. The limitation to the equatorial observer is motivated by the fact that the most important candidate black hole, Sgr A*, is likely to have a spin axis perpendicular to the galactic plane, where the solar system lies, in a first approximation. It is natural, then, to take advantage of this configuration and deal with considerably simplified equations.

Our paper is structured as follows. Section II recalls the main results of Kerr geodesics. Section III explains how the SDL is introduced in Kerr gravitational lensing and illustrates the strategy we use to solve the geodesics equations. Section IV contains the derivation of the caustics order by order. In Section V we analyze the lens map close to the relativistic caustics, finding the additional images and their magnification. Section VI considers the perspectives for observations in the light of what we have found, focusing on the study of relativistic images around Sgr A*. Section VII summarizes the main results of the paper. Two appendices complement the calculations explained in Section III with more details.

II. KERR GEODESICS

In Boyer-Lindquist coordinates [29] $x^\mu \equiv (t, x, \vartheta, \phi)$, the Kerr metric reads

$$ds^2 = \frac{\Delta - a^2\sin^2\vartheta}{\rho^2}dt^2 - \frac{\rho^2}{\Delta}dx^2 - \rho^2 d\vartheta^2 - \frac{(x^2+a^2)^2 - a^2\Delta\sin^2\vartheta}{\rho^2}\sin^2\vartheta d\phi^2 + \frac{2ax\sin^2\vartheta}{\rho^2}dtd\phi, \tag{1}$$

$$\Delta = x^2 - x + a^2, \tag{2}$$

$$\rho^2 = x^2 + a^2\cos^2\vartheta, \tag{3}$$

where a is the specific angular momentum of the black hole. All distances are measured in Schwarzschild radii ($2MG/c^2 = 1$). ϑ and ϕ represent the polar and azimuthal angles, respectively, while x is the radial coordinate. The event horizon is a spherical surface of radius $x_H = (1 + \sqrt{1-4a^2})/2$. In our notations, a runs from 0 (Schwarzschild black hole) to $1/2$ (extremal Kerr black hole).

Carter showed that the Kerr geodesics can be resolved in terms of first integrals of motion [22]. The final expressions for lightlike geodesics take the following form (following Ref. [23])

$$\pm\int\frac{dx}{\sqrt{R}} = \pm\int\frac{d\vartheta}{\sqrt{\Theta}}, \tag{4}$$

$$\phi_f - \phi_0 = a\int\frac{x^2+a^2-aJ}{\Delta\sqrt{R}}dx - a\int\frac{dx}{\sqrt{R}} + J\int\frac{\csc^2\vartheta}{\sqrt{\Theta}}d\vartheta, \tag{5}$$

where

$$\Theta = Q + a^2\cos^2\vartheta - J^2\cot^2\vartheta, \tag{6}$$

$$R = x^4 + (a^2 - J^2 - Q)x^2 + (Q + (J-a)^2)x - a^2Q. \tag{7}$$

In these expressions, J and Q are two constants of motion that, along with the initial condition ϕ_0, completely identify the geodesic. The double signs in front of the integrals in Eq. (4) remind that the integrals must be performed piecewise, between two consecutive values of x and ϑ

that annihilate the denominators R and Θ (inversion points). Then the sign of each piece between two inversion points is chosen in such a way that all of them sum up with the same sign, giving a final positive contribution.

In the context of gravitational lensing, we are interested to those photons that come from an infinite distance, approach the black hole reaching a minimum distance x_0, and then escape back to infinity. This selects trajectories characterized by $Q \geq 0$. Moreover, since the roots of R represent inversion points in the radial motion, we have to impose that R has one nondegenerate positive root. This amounts to require that $R(x_0) = 0$, $R'(x_0) \neq 0$. The limiting situation, when x_0 becomes a degenerate root, is obtained when the equations $R(x_m) = 0$, $R'(x_m) = 0$ are simultaneously fulfilled at some point x_m. Solving these equations w.r.t. J and Q we get

$$J_m = \frac{x_m^2(-3 + 2x_m) + a^2(1 + 2x_m)}{a(1 - 2x_m)}, \tag{8}$$

$$Q_m = \frac{x_m^3[2a^2 - x_m(x_m - 3/2)^2]}{a^2(x_m - 1/2)^2}. \tag{9}$$

Given a value of x_m, the quantities J_m and Q_m represent the values of J and Q that characterize those trajectories that bring a photon down to the distance x_m in an infinite time. Asymptotically the photon keeps orbiting forever at a fixed distance x_m from the black hole. However, this orbit is unstable and small perturbations make the photon fall into the black hole or deviate it back to infinity. In Schwarzschild black hole, the radius x_m of the unstable photon orbit is fixed to $3/2$ in Schwarzschild units (the sphere of radius x_m is then called photon sphere). In the case of Kerr black holes, the radius of the orbit depends on the initial orientation of the photon trajectory. In practice, x_m may vary between two limiting values x_{m+}, x_{m-}, which, respectively, represent the radius of the orbit described by a photon corotating with the black hole and the radius of the orbit of a counterrotating photon in the equatorial plane. All intermediate values correspond to photons whose orbits are not equatorial and do not lie on a single plane. In order to find these limiting values, we have to impose $Q_m = 0$. So, x_{m+} and x_{m-} are found as the two largest roots of this equation. This is a third degree equation whose solution can be found exactly. However, since the successive calculations would soon become too cumbersome, we will already consider their expansions in powers of a. To describe second order effects in the lens equation, it is necessary to take terms up to the third order:

$$x_{m\pm} = \frac{3}{2} \mp \frac{2}{\sqrt{3}}a - \frac{4}{9}a^2 \mp \frac{20}{27\sqrt{3}}a^3 + O(a^4). \tag{10}$$

We see that in the limit $a \to 0$, the two limiting values converge to the Schwarzschild photon sphere $x_m = 3/2$. When a is different from zero, x_{m+} and x_{m-} are distinct. The specific value of x_m in the interval $[x_{m+}, x_{m-}]$ uniquely fixes the amplitude of the oscillations on the equatorial plane performed by the photon along its orbit. In consideration of this fact we introduce a more convenient parametrization, replacing a by $a\xi$:

$$x_m(\xi) = \frac{3}{2} - \frac{2}{\sqrt{3}}a\xi - \frac{4}{9}a^2\xi^2 - \frac{20}{27\sqrt{3}}a^3\xi^3. \tag{11}$$

Varying the parameter ξ in the range $[-1, 1]$ we obtain all possible values of x_m in the range $[x_{m+}, x_{m-}]$, corresponding to orbits with different amplitudes of the oscillations on the equatorial plane (a different parameterization with similar properties was used in Ref. [30]). We shall see that all quantities assume very simple expressions in terms of this parameter ξ. Now, using this parametrization in Eqs. (8) and (9), we can expand J_m and Q_m to second order in a and read them as functions of ξ:

$$J_m(\xi) = \frac{3\sqrt{3}}{2}\xi - 2a - \frac{a^2\xi(2 - \xi^2)}{\sqrt{3}} + O(a^3), \tag{12}$$

$$Q_m(\xi) = \frac{27}{4}(1 - \xi^2) + 3a^2\xi^2(1 - \xi^2) + O(a^3). \tag{13}$$

Notice that the presence of a in the denominators of Eqs. (8) and (9) allows ξ to appear at zero order already. That is why we needed a third order expansion for x_m. So, even in the Schwarzschild limit, ξ can be used to parametrize the photon sphere in the (J, Q) plane.

In Fig. 1 we plot the locus of points (J_m, Q_m) when we vary ξ in the range $[-1, 1]$, for different values of a. We recall that purely prograde photons travelling on the equatorial plane are characterized by $Q = 0$ and positive J, while retrograde photons have negative J. Photons with $J = 0$ and $Q > 0$ run on polar trajectories. Any geodesics characterized by J and Q outside this locus (with $Q \geq 0$), correspond to acceptable gravitational lensing trajectories.

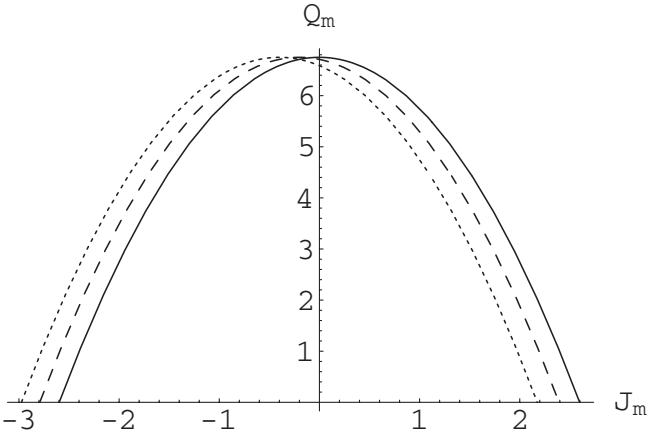

FIG. 1. The limiting values J_m and Q_m for the constants of motion J and Q corresponding to trajectories reaching the unstable orbit around the black hole asymptotically. The solid line is for $a = 0$, the dashed line is for $a = 0.1$, and the dotted line is for $a = 0.2$.

All photons with J and Q inside this locus are destined to fall inside the black hole.

There is an immediate connection between these constants and the point in the sky where the observer detects the photon. Throughout the paper, we consider a static observer at a radial Boyer-Lindquist coordinate D_{OL}, lying on the equatorial plane. This restriction will keep all equations simple enough to be solved, while ensuring an exhaustive description of the expected phenomenology for Sgr A*. This definition has no ambiguity from a mathematical point of view, but needs to be linked to the astrophysical notion of distance from the solar system to Sgr A*. The current measurements of the distance to the Galactic center are typically based on the dynamical investigation of the stars orbiting around Sgr A*. The orbital fits are done in the context of Newtonian gravity. As a consequence, the current estimate of the distance to the Galactic center, which amounts to about 8 kpc [2,31], assumes a flat background geometry. This flat distance makes sense as long as all scales are much larger than the Schwarzschild radius of the central black hole, which is

$$R_{\rm Sch} = \frac{2GM}{c^2} = 1.1 \times 10^{10}\ {\rm m} \tag{14}$$

for $M = 3.61 \times 10^6\ {\rm M}_\odot$ [2]. Now it is evident that in the limit of large distances, one can simply translate any flat distance from the black hole, as calculated by Newtonian physics, into Boyer-Lindquist coordinates in the Kerr geometry. In fact, far from the black hole, in the asymptotic region, the Boyer-Lindquist coordinate coincides with the Euclidean spherical coordinates centered on the black hole. The ambiguity in this identification is of the order of $R_{\rm Sch}/x$ (x being the distance from the black hole) and becomes relevant only close to the event horizon, where Newtonian physics loses any meaning. So, we can safely assume $D_{OL} = 8$ kpc, when speaking about Sgr A* in any calculations.

Then, considering only observers in the asymptotic region ($D_{OL} \gg 1$), where the geometry is close to be Minkowskian, it is possible to define angular coordinates (θ_1, θ_2) in the observer sky. We will put the black hole in (0,0), and let θ_1 run parallel to the equatorial plane of the black hole while θ_2 will run on the perpendicular axis (see Fig. 2). As $D_{OL} \gg 1$, θ_1 and θ_2 will always be assumed to be very small. As shown in Ref. [23], photons reaching the observer from the generic point (θ_1, θ_2) are characterized by the constants

$$J = -\theta_1 D_{OL}, \tag{15}$$

$$Q = \theta_2^2 D_{OL}^2, \tag{16}$$

w.r.t. to the black hole. We have taken the spin axis of the black hole parallel to the θ_2 direction and we have considered a photon moving toward the observer. Then, it is immediate to pass from (J, Q) to the corresponding coordinates in the observer sky (θ_1, θ_2) and vice versa, apart from an ambiguity of sign in θ_2.

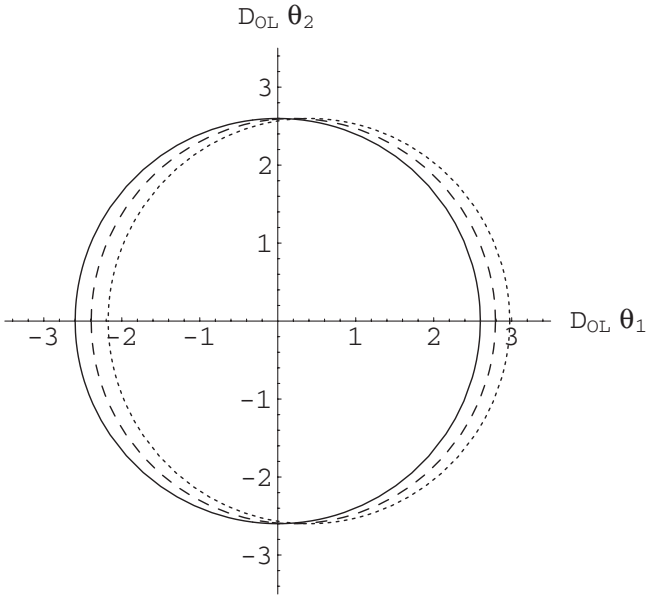

FIG. 2. The shadow shape in the observer sky. The solid line is for $a = 0$, the dashed line is for $a = 0.1$, and the dotted line is for $a = 0.2$.

We can use these formulae to translate the locus (J_m, Q_m) into a new one $(\theta_{1,m}, \theta_{2,m})$ in the plane (θ_1, θ_2). This is given by

$$D_{OL}\theta_{1,m}(\xi) = -\frac{3\sqrt{3}\xi}{2} + 2a + \frac{a^2\xi(2-\xi^2)}{\sqrt{3}} + O(a^3), \tag{17}$$

$$D_{OL}\theta_{2,m}(\xi) = \pm\left(\frac{3\sqrt{3}}{2} + \frac{a^2\xi^2}{\sqrt{3}}\right)\sqrt{1-\xi^2} + O(a^3), \tag{18}$$

and is called the shadow of the black hole.

Figure 2 shows the shape of the shadow in the observer sky for different values of a. From what we have said before, all photons deflected by the black hole must reach the observer from directions (θ_1, θ_2) outside the shadow. Photons reaching the observer from the inside of the shadow cannot come from gravitational deflection but must have been generated by sources in front of the black hole. So, if we had enough resolution to fully image a black hole, we would see a black shadow with the shape described by Eqs. (17) and(18), bordered by a luminous ring due to gravitational lensing of all sources around the black hole [6].

In Fig. 2 we see that the Schwarzschild shadow is circular. Increasing the black hole spin a, the shadow is slightly distorted and gets displaced to the right, meaning that prograde photons (coming from the left side as seen from the observer) are allowed to get closer to the black

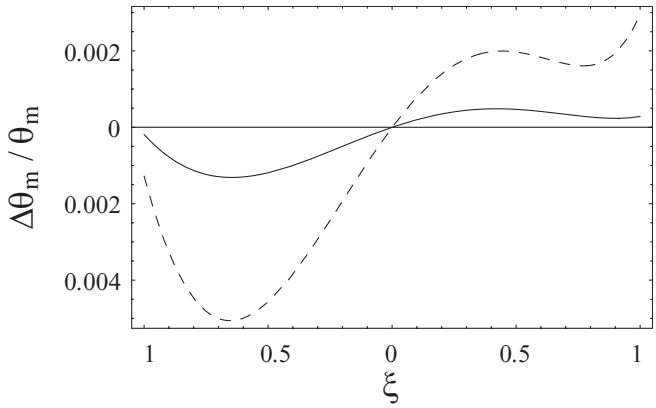

FIG. 3. The relative variation in the radial distance of the black hole shadow shape between the exact solution and the second-order approximation as a function of the azimuthal variable ξ. The solid line is for $a = 0.1$, the dashed line is for $a = 0.2$.

hole, while retrograde photons (coming from the right side) must keep farther.

Here, for later convenience, we are introducing and making use of expressions expanded to the second order in a. However, the exact expression for the shadow can be easily derived, combining Eqs. (8) and (9) with Eqs. (15) and (16). Comparing the exact shadow to its second order approximation, we find that the latter works surprisingly well up to very high values of the black hole spin. In Fig. 3, we plot the relative error in the radial angular distance of the apparent shadow θ_m in the approximate solution w.r.t the exact one as a function of the variable ξ, which follows the azimuthal angle in the observer's sky. Up to $a \lesssim 0.28$, relative variations are well under 1%, at $a = 0.4$ we find an error of 2%, while in the extremal case $a = 0.5$ the error only reaches 5%. Such errors must be compared to the displacement of the relativistic rings from the shadow, see Section IV, and turn out to be negligible for the higher order critical curves up to large values of the spin.

III. KERR LENSING IN THE STRONG DEFLECTION LIMIT

It is useful to introduce the following parametrization:

$$\begin{cases} \theta_1(\epsilon, \xi) = \theta_{1,m}(\xi)(1 + \epsilon) \\ \theta_2(\epsilon, \xi) = \theta_{2,m}(\xi)(1 + \epsilon) \end{cases}. \tag{19}$$

Varying ξ in the range $[-1, 1]$ and ϵ in the range $[-1, \infty]$, we can obviously cover the whole upper half of the observer sky, since ξ establishes the anomaly of the light ray w.r.t. a reference axis in the sky (through Eqs. (17) and (18)) and ϵ fixes the angular distance from the center of the black hole.

In this paper, we are interested in light rays experiencing very large deflections by a Kerr black hole. These light rays reach the observer from directions (θ_1, θ_2) very close to the shadow. In the parametrization (19), they are thus described by light rays with very small positive ϵ, while keeping ξ in the whole range $[-1, 1]$. The SDL amounts to performing the integrals in the geodesics Eqs. (4) and (5), to the lowest orders in ϵ.

Now, we can easily derive the values of J and Q for these strongly deflected photons using Eqs. (15) and (16):

$$J(\xi, \epsilon) = J_m(\xi)(1 + \epsilon), \tag{20}$$

$$Q(\xi, \epsilon) = Q_m(\xi)(1 + 2\epsilon). \tag{21}$$

Substituting these expressions in Eq. (7) and solving the equation $R = 0$ for x_0, we get the closest approach distance as

$$x_0(\xi, \delta) = x_m(\xi)(1 + \delta), \tag{22}$$

$$\delta = \sqrt{\frac{2\epsilon}{3}}\left[1 - \frac{2}{3\sqrt{3}}a\xi - \frac{8}{27}a^2(4\xi^2 - 3)\right]. \tag{23}$$

In general, we see that the relation between δ and ϵ depends on ξ, contrary to what happens in the Schwarzschild case, which, by the way, is correctly recovered when a is set to zero (compare with Ref. [17]). In the resolution of the geodesics equation we will mostly use δ rather than ϵ. However, they can be immediately interchanged by Eq. (23) and its inverse.

A. Resolution strategy

Let us introduce our gravitational lensing configuration. As said before, we restrict to observers on the equatorial plane of the black hole at radial coordinate D_{OL}. We choose the zero of the azimuthal Boyer-Lindquist coordinate ϕ on the observer position. The source is assumed to be static at Boyer-Lindquist coordinates $(D_{LS}, \vartheta_s, \phi_s)$. To make contact with previous works, we call $\gamma = \phi_s - \pi$.

Our lens equations are provided by Eqs. (4) and (5), where we identify $\phi_f = 0$, $\phi_0 = \phi_s$. In these equations there are four different integrals to solve:

$$I_1 = 2\int_{x_0}^{\infty} \frac{dx}{\sqrt{R}}, \tag{24}$$

$$I_2 = 2\int_{x_0}^{\infty} \frac{x^2 + a^2 - aJ}{\Delta\sqrt{R}}\,dx, \tag{25}$$

$$J_1 = \pm\int \frac{1}{\sqrt{\Theta}}\,d\vartheta, \tag{26}$$

$$J_2 = \pm\int \frac{csc^2\vartheta}{\sqrt{\Theta}}\,d\vartheta. \tag{27}$$

In the radial integrals I_1 and I_2 we have taken the higher extrema to be infinite, because we assume $D_{OL}, D_{LS} \gg 1$. As the two integrands go to zero as x^{-2} for $x \to \infty$, the relative errors committed in this approximation are of order

D_{OL}^{-1} and D_{LS}^{-1}, respectively. Moreover, since the only inversion point in the radial motion is x_0, the infalling pieces and the outgoing pieces of the integral are equal and we can solve the sign ambiguity considering only the outgoing pieces and putting a factor 2 in front of the integrals. The radial integrals I_1 and I_2 can then be solved using the SDL technique explained in Ref. [17]. In practice, considering photons with minimum distance very close to some x_m, and introducing the parametrizations (20), (21), (22), we can expand the integrals in terms of the parameter δ, introduced before. The leading terms diverge logarithmically as δ goes to zero, while the next-to-leading order terms are constants in δ. The details of this procedure are reported in Appendix A. Here we just rewrite the final results

$$I_1 = -a_1 \log\delta + b_1, \tag{28}$$

$$I_2 = -a_2 \log\delta + b_2, \tag{29}$$

where the coefficients a_i and b_i are functions of a and ξ. Their expansions to second order in a are reported in Appendix A.

As regards the angular integrals (26) and (27), it is convenient to introduce the new variable $\mu = \cos\vartheta$. The final results, expanded to second order in a are functions of ξ and the source position $\mu_s = \cos\vartheta_s$. They are reported with a full derivation in Appendix B. We will just recall them in the following sections when we need them.

Once all integrals are calculated, we have to solve Eqs. (4) and (5) in terms of the source coordinates (γ, μ_s), so that they are in the lens map form

$$\begin{cases} \mu_s = \mu_s(\delta, \xi) \\ \gamma = \gamma(\delta, \xi) \end{cases}. \tag{30}$$

Since all transformations from (γ, ϑ_s) to (γ, μ_s) and from (θ_1, θ_2) to (δ, ξ) are nonsingular (except for the points $\xi = \pm 1$), the singularities of the Jacobian of the map (30) represent gravitational lensing critical points.

In the following sections, we will calculate the critical curves and the caustics of the Kerr gravitational lens order by order. Then we will describe the lens mapping in a neighborhood of a generic caustic, deriving the images position and magnification.

IV. DERIVATION OF THE RELATIVISTIC CAUSTICS

A. Zero-order caustics

Sending a to zero, we must recover the Schwarzschild results, i.e. that critical curves are concentric rings corresponding to pointlike caustics aligned on the optical axis, alternatively located behind and in front of the black hole. Of course, as $a \to 0$, all expressions are considerably simplified, and it is possible to follow calculations without too much effort.

Reading all the zero-order results for the integrals in Appendices A and B, Eq. (4) becomes

$$-2\log\delta + 2\log[12(2-\sqrt{3})] = \pm \arcsin\frac{\mu_s}{\sqrt{1-\xi^2}} + m\pi. \tag{31}$$

Defining the new variable

$$\psi = -2\log\delta + 2\log[12(2-\sqrt{3})], \tag{32}$$

Eq. (31) can be easily solved as

$$\mu_s = \pm\sqrt{1-\xi^2}\,\sin\psi. \tag{33}$$

The second lens equation (5) now reads

$$\gamma = -(m-1)\pi \mp \arctan\frac{\mu_s\xi}{\sqrt{1-\mu_s^2-\xi^2}}. \tag{34}$$

Using Eq. (33) to eliminate μ_s, we find

$$\gamma = -(m-1)\pi - \arctan[\xi\tan\psi]. \tag{35}$$

The number m appearing in this equation is the integer part of $(\psi/\pi + 1/2)$ and must be interpreted as the number of inversions in the polar motion of the photon.

Equations (33) and (35) represent the lens equations for a Schwarzschild black hole without the classical identification of the equatorial plane with the source-lens-observer plane. We can recover the results of Ref. [17] imposing that the motion takes place on the equatorial plane, i.e. setting $\xi = 1$. Then we have $\mu_s = 0$ (the source must coherently lie on the equatorial plane) and $\gamma = -\psi + \pi$. The quantity $\psi - \pi$ represents the deflection angle of a photon approaching the Schwarzschild black hole at a distance $x_0 = x_m(1+\delta)$. Equations (33) and (35) can also be obtained from the traditional planar treatment by a trivial rotation by an angle $\arccos\xi$ of the reference plane around the optical axis using some spherical trigonometry.

Now we can easily calculate the Jacobian of our lens map. We find

$$\frac{\partial\mu_s}{\partial\xi} = \mp\frac{\xi}{\sqrt{1-\xi^2}}\,\sin\psi, \tag{36}$$

$$\frac{\partial\mu_s}{\partial\psi} = \pm\sqrt{1-\xi^2}\,\cos\psi, \tag{37}$$

$$\frac{\partial\gamma}{\partial\xi} = -\frac{\tan\psi}{1+\xi^2\tan^2\psi}, \tag{38}$$

$$\frac{\partial\gamma}{\partial\psi} = -\frac{\xi\sec^2\psi}{1+\xi^2\tan^2\psi}, \tag{39}$$

and

$$D = \frac{\partial\mu_s}{\partial\xi}\frac{\partial\gamma}{\partial\psi} - \frac{\partial\mu_s}{\partial\psi}\frac{\partial\gamma}{\partial\xi} = \pm\frac{\sin\psi}{\sqrt{1-\xi^2}}. \tag{40}$$

The critical curves are the solutions of the equation $D = 0$, which, in our case, simply gives

$$\psi_{cr} = k\pi. \tag{41}$$

The critical ψ does not depend on ξ. Recalling that ψ is just a function of δ expressed by Eq. (32), we have

$$\delta_{cr} = 12(2 - \sqrt{3})e^{-k\pi/2}. \tag{42}$$

Switching to ϵ by Eq. (23), we have

$$\epsilon_{cr} = 216(2 - \sqrt{3})^2 e^{-k\pi}. \tag{43}$$

Then, recalling the meaning of ϵ by Eq. (19) and taking $\theta_{1,m}$ and $\theta_{2,m}$ from Eqs. (17) and (18), we finally find

$$\begin{aligned} D_{OL}\theta_{1,cr}(\xi) &= -\frac{3\sqrt{3}\xi}{2}[1 + \epsilon_{cr}(k)], \\ D_{OL}\theta_{2,cr}(\xi) &= \pm\frac{3\sqrt{3}}{2}\sqrt{1 - \xi^2}[1 + \epsilon_{cr}(k)], \end{aligned} \tag{44}$$

that is a series of rings parameterized by ξ, slightly larger than the shadow of the black hole, in full agreement with Refs. [1,13,14,17]. The critical curves are labeled by the number k. We shall refer to k as the critical curve order or the caustic order, when we consider the corresponding caustic.

Coming to the caustics, inserting Eq. (41) in the lens equations (33)–(35) and noting that the number of inversions in polar motion is $m = k$, we find

$$\mu_s = 0, \qquad \gamma = -(k - 1)\pi. \tag{45}$$

The caustics are points aligned on the optical axis. For odd k they are behind the black hole, while for even k they are in front of the black hole (retrolensing caustics). In the Schwarzschild limit, the number of loops performed by photons forming critical images of order k is just $(k - 1)/2$. However, this is not exactly true for spinning black holes, as we shall see in the next section. So, it is better to think of the order of the critical curve k as the number of inversions in the polar motion done by photons associated to it.

Of course, the first caustic for $k = 1$ is the classical weak field limit one, which is outside the range of the SDL approximation, so we cannot expect to recover the Einstein ring radius putting $k = 1$ into Eq. (44) (the first caustic is no longer described even by the weak field approximation if the source is close to the black hole). However, as shown in Refs. [7,17], the SDL approximation works better and better for higher k, starting from the first retrolensing caustic in $k = 2$. It is these caustics that we are going to study in the following sections. In particular, we will find out how they are displaced and deformed by the black hole spin, obtaining a full analytic description of their shape.

B. First-order caustics

Up to now we have just reobtained all the Schwarzschild black hole results in a more complicated form, starting from Kerr geodesics equations and sending a back to zero. Now, we shall introduce first-order corrections to our lens equations, rederiving the critical curves and the caustics. We anticipate that the caustics get displaced from the optical axis in the azimuthal direction, though remaining pointlike.

Using the first order terms of the radial and angular integrals from the Appendices A and B, we can add the terms proportional to a in the Eqs. (33) and (35). The inversion of the μ_s equation can be easily performed order by order in a. Then, repeating the same steps of the previous section, we find

$$\mu_s = \pm\sqrt{1 - \xi^2}\sin\psi \pm \frac{4a\xi}{3\sqrt{3}}\sqrt{1 - \xi^2}\sin\psi, \tag{46}$$

$$\begin{aligned} \gamma = &-(m - 1)\pi - \arctan[\xi\tan\psi] \\ &- \frac{4a}{3\sqrt{3}}\left[\psi + \frac{\xi^2\tan\psi}{1 - (1 - \xi^2)\sin^2\psi} - \tan\psi \right. \\ &\left. + 3\sqrt{3}\log(2\sqrt{3} - 3)\right]. \end{aligned} \tag{47}$$

Note that for ψ close to $m\pi + \pi/2$ and ξ close to zero, the first order correction to μ_s may bring it to absolute values larger than 1. As μ_s is the cosine of the polar angle, these values are unphysical. This inconsistency comes out because, when we solve for μ_s order by order, we expand the arcsin function in points very close to the extrema of its definition range, where the arcsin is not analytic. Then, the linear approximation obviously takes us out of the interval $[-1, 1]$. The dangerous values of ψ and ξ correspond to nearly polar trajectories where the final direction is very close to 1 of the two poles. However, as we shall see, the highest magnification for the relativistic images is obtained when the source is close to a caustic. Luckily, the caustics lie at $\mu \simeq 0$ for an equatorial observer, so that we will always work very far from these dangerous regions. This danger will become effective for very high order caustics, which may become very large, as we shall see in the next subsection.

Now we can calculate the derivatives of the lens equation as before. The Jacobian reads

$$D = \pm\frac{\sin\psi}{\sqrt{1 - \xi^2}}\left(1 + \frac{8a\xi}{3\sqrt{3}}\right), \tag{48}$$

which tells us that the critical curves are still described by Eq. (41) even at first order. This means that there is no correction to the critical δ (42) of the previous section. The fact that we do not get any corrections to δ does not mean that the shape of the critical curves is not altered by the black hole spin at first order. Indeed going back from δ to ϵ we get a first-order correction, according to Eq. (23).

Moreover, the shadow shape is modified according to Eqs. (17) and (18). Then, to first order, the critical curves are

$$D_{OL}\theta_{1,cr}(\xi) = -\frac{3\sqrt{3}\xi}{2}(1+\epsilon_{cr}) + 2a[1+\epsilon_{cr}(1-\xi^2)],$$
$$D_{OL}\theta_{2,cr}(\xi) = \pm\frac{3\sqrt{3}}{2}\sqrt{1-\xi^2}[1+\epsilon_{cr}] \pm 2a\epsilon_{cr}\xi\sqrt{1-\xi^2}, \quad (49)$$

with ϵ_{cr} still given by Eq. (43).

Also the caustics are modified. In fact, plugging $\psi_{cr} = k\pi$ into Eqs. (46) and (47), we find

$$\mu_s = 0, \quad (50)$$

$$\gamma = -(k-1)\pi - 4a\left[\frac{k\pi}{3\sqrt{3}} + \log(2\sqrt{3}-3)\right]. \quad (51)$$

The caustics are still fully confined to the equatorial plane, they are still pointlike, but they are displaced from the optical axis. The displacement is negative, which means that the caustics drift clockwise if we look at the Kerr black hole from the northern pole. So, we can say that if a source lies on a caustic point of order k, prograde light rays perform more than $(k-1)/2$ loops while retrograde light rays perform less than $(k-1)/2$ loops. The number of inversions in the polar motion is still k. Higher-order caustics are more displaced, because of the k dependence in Eq. (51). Of course, as said before, this formula correctly describes all caustics except for the weak field one, corresponding to $k = 1$. Going to second order in a we will describe the full shape of the caustics.

C. Second-Order Caustics

At first order in a the caustics still remain pointlike, while it is known that they get a finite extension when a is different from zero [26,27]. So, it is necessary to proceed to second order. To the right-hand side of Eqs. (46) and (47) we have to add the following quantities, respectively:

$$\delta\mu_s^{(2)} = \pm\frac{\sqrt{1-\xi^2}}{108\sqrt{3}}a^2[12\sqrt{3}(1-\xi^2)\psi_n\cos\psi - \sqrt{3}(1+31\xi^2)\sin\psi - \sqrt{3}(1-\xi^2)\sin 3\psi], \quad (52)$$

$$\delta\gamma^{(2)} = \frac{2a^2}{27\xi^2}(1-\xi^2)(23\xi^2-4)\arctan(\xi t) + \frac{2}{9}a^2\xi(16-\psi_n) - \frac{1-\xi^2}{9(1+\xi^2t^2)}a^2\xi\left[(1+t^2)\psi_n + \frac{t}{3}\left(23-\frac{8}{\xi^2}-16\frac{1+t^2}{1+\xi^2t^2}\right)\right], \quad (53)$$

where $t = \tan\psi$ and $\psi_n = 5\psi + 8\sqrt{3} - 20$.

Note that a term directly proportional to ψ appears in Eq. (52) through ψ_n. This is another danger for the approximation, since for very large ψ, i.e. photons performing several loops around the black hole, $\delta\mu_s^{(2)}$ may become even larger than 1. This breakdown sets the true limit to the applicability range of the perturbative expansion in a, which gets smaller and smaller for photons making many loops. However, the brightest images are formed by photons associated to critical images of low order. For these images, as we shall see, the range of applicability of the perturbative expansion is considerably large.

Now let us find out the corrections to the critical curves. Once we have calculated all derivatives of the lens equations and written the Jacobian to the second order in a, we set

$$\psi = k\pi + a^2\delta\psi, \quad (54)$$

as we already know the zero-order critical curve and we know that there is no correction at the first order. Then we easily get rid of all the trigonometric functions and the final Jacobian reads

$$D = \pm\frac{(-1)^k a^2}{9\sqrt{1-\xi^2}}[9\delta\psi - (92-24\sqrt{3}-15k\pi)(1-\xi^2)]. \quad (55)$$

The $(-1)^k$ is a consequence of the expansions of the trigonometric functions, while the double sign inherited by the Jacobian at all orders depends on the fact that the (ϵ, ξ) parametrization only covers half of the observer sky and we are forced to introduce a double sign in the equation for μ_s.

The equation $D = 0$ gives the second order correction to the critical ψ in a very simple form

$$\delta\psi = \frac{92-24\sqrt{3}-15k\pi}{9}(1-\xi^2). \quad (56)$$

Now we can remount the complete second-order expansion of the critical curves, which reads

$$D_{OL}\theta_{1,cr}(\xi) = -\frac{3\sqrt{3}\xi}{2}(1+\epsilon_{cr}) + 2a[1+\epsilon_{cr}(1-\xi^2)] - \frac{\xi a^2}{\sqrt{3}}\left\{\xi^2 - 2 + \left[\frac{15}{2}k\pi(1-\xi^2) + \frac{176}{3} - 12\sqrt{3} + \left(\frac{179}{3}-12\sqrt{3}\right)\xi^2\right]\epsilon_{cr}\right\},$$
$$D_{OL}\theta_{2,cr}(\xi) = \pm\frac{3\sqrt{3}}{2}\sqrt{1-\xi^2}[1+\epsilon_{cr}] \pm 2a\epsilon_{cr}\xi\sqrt{1-\xi^2} \pm \frac{\sqrt{1-\xi^2}}{\sqrt{3}}a^2\left\{\xi^2 + \left[\frac{15}{2}k\pi(1-\xi^2) + 12\sqrt{3} - 54 + \left(\frac{179}{3}-12\sqrt{3}\right)\xi^2\right]\epsilon_{cr}\right\}. \quad (57)$$

Here, again, we have $k\pi$ terms which become large for higher-order critical curves.

Finally, let us calculate the caustics at the second order in a. Plugging Eq. (54) with (56) into the lens equations, we find

$$\mu_s = \pm(-1)^k r_c (1 - \xi^2)^{3/2}, \tag{58}$$

$$\gamma = -(k-1)\pi - 4a\left[\frac{k\pi}{3\sqrt{3}} + \log(2\sqrt{3} - 3)\right] + r_c \xi^3, \tag{59}$$

where we define

$$r_c = \frac{2}{9} a^2 (5k\pi + 8\sqrt{3} - 36). \tag{60}$$

The analytical expressions of the Kerr black hole caustics, given by Eqs. (58) and (59) to the second order in the black hole spin a, represent a major achievement of this paper. Before discussing their shape and all the physical implications, it is a good idea to test our formulae by comparing them to the results obtained by alternative methods. In Ref. [27], the intersections of the caustics with the equatorial plane were found using the SDL approximation only, without any limitation for the black hole spin. The first test is to analytically expand the formulae of Ref. [27] to the second order in a, without using any numerical integrations. Indeed, we get the same expressions as in Eq. (59), evaluated for $\xi = \pm 1$. Furthermore, we can draw in the same plot the intersections of the caustics with the equatorial plane as calculated in this paper along with those calculated in Ref. [27]. Rather than making two separate plots for prograde and retrograde photons, we can make a unique plot, letting a vary in the range $[-0.5, 0.5]$ and keeping the values of Eq. (59) for $\xi = 1$. So, the left side of the plot ($a < 0$) represents the intersections for retrograde photons and the right side ($a > 0$) represents the intersections of prograde photons. We see in Fig. 4 that the second-order approximations (dashed lines) follow the exact expressions of Ref. [27] very accurately. We can estimate that for lower-order caustics the perturbative approximation works up to $a \simeq 0.3$, while for the last caustic in the plot ($k = 7$) we have to stop at $a \simeq 0.1$. In any case, the validity range is impressively large, reaching values of the black hole spin comparable to the extremal case. This encourages us to make extensive and confident use of the second-order approximation for a full description of Kerr lensing phenomenology.

Now, let us discuss the shape and the extension of Kerr lensing caustics. Looking at Eq. (58), it is interesting to note that the upper half of the critical curve is mapped in the lower half of the caustic for odd k, while it is mapped in the upper half if k is even. As already found numerically in Ref. [26], the caustics have the characteristic astroid shape shown in Fig. 5, common to all tangential caustics after the breaking of the axial symmetry. The four cusps are in $\xi = \pm 1$ and $\xi = 0$ choosing different signs for μ_s.

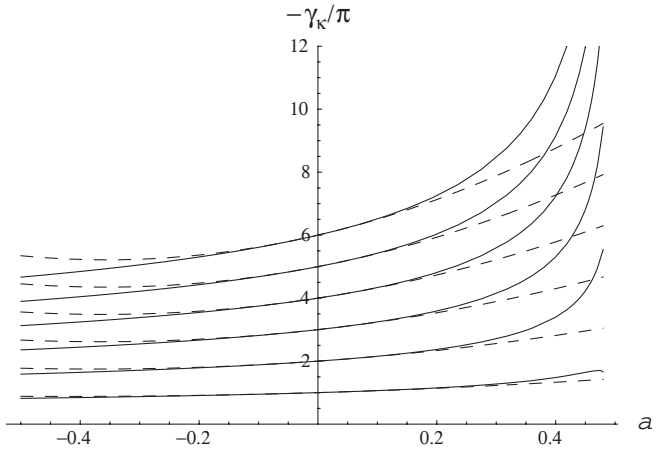

FIG. 4. Comparison between the intersections of the caustics with the equatorial plane as calculated in Ref. [27] without the perturbative approximation for the black hole spin (solid lines) and the ones calculated in the present paper (dashed lines). The plot refers to the caustics of order $2 \leq k \leq 7$.

The caustics have the same extension in γ and μ. We recall that γ is just the azimuthal angle of the Boyer-Lindquist coordinates taken from the reference axis starting from the black hole and going in the direction opposite to the observer, while μ is the cosine of the polar angle ϑ. As said before, we can trust our results as long as the

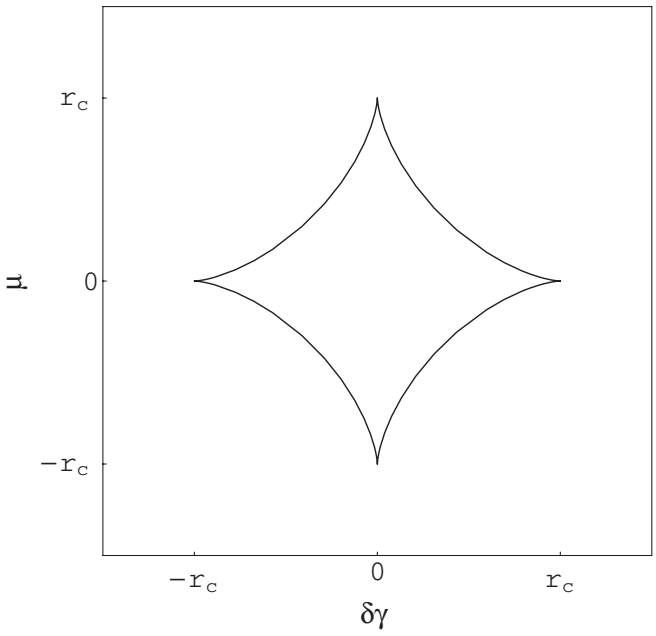

FIG. 5. The typical caustic in Kerr gravitational lensing has the astroid shape and the same angular extension r_c (given by Eq. (60)) along the azimuthal and the polar direction.

TABLE I. Drift (in radians) of the caustics of order k with $2 \leq k \leq 7$, for different values of a.

	a = 0.01	a = 0.05	a = 0.1	a = 0.2
$\Delta\gamma_2$	0.018	0.088	0.18	0.35
$\Delta\gamma_3$	0.042	0.21	0.42	0.84
$\Delta\gamma_4$	0.066	0.33	0.66	1.3
$\Delta\gamma_5$	0.09	0.45	0.9	1.8
$\Delta\gamma_6$	0.11	0.57	1.14	2.3
$\Delta\gamma_7$	0.14	0.69	1.39	2.8

perturbative terms remain small. In this regime, $\mu \simeq \frac{\pi}{2} - \vartheta$. Then, we deduce that the caustics have the same extension in the azimuthal and in the polar direction.

The extension is parameterized by the quantity r_c, which is the semiaxis of the caustic. We see that it grows with the black hole spin a and with the caustic order k. Thus, for higher caustic orders, the perturbative approximation fails for smaller and smaller values of a, while it remains good for lower order caustics. This was already noted while commenting Fig. 4.

The drift from the optical axis of the caustic is given by the first order term in Eq. (59). Indicating it by $\Delta\gamma$, in Table I we report the obtained values for the first 6 relativistic caustics, starting from $k = 2$, for values of the black hole spin going up to $a = 0.2$. We see that the drift may become very large, amounting to several radians already for the fifth-order caustic, while still in a regime where the perturbative solution is valid. For higher-order caustics, the number of loops may be significantly different from the planar orbit result $(k - 1)/2$. Another important consideration is that we do not need perfect alignment between source, lens, and observer to have gravitational lensing. To enhance the images associated with a critical curve of order k, the source must align with the corresponding order k caustic, which may be well off the optical axis. Moreover, the relativistic images are not enhanced all at the same time, since caustics of different order move far away from each other.

In Table II we report the radii of the first 6 relativistic caustics for different values of a. The extension of the caustics is of second order in a and thus remains much smaller than the drift, reaching some tenth of radians in the perturbative regime. Outside of this regime, it is difficult to know what would happen to higher-order caustics. Would their vertical extension saturate before reaching the poles or would they wrap around the pole? Would they meet each other and make transitions to more complicated structures? The answers to these questions need further research, both analytically and numerically. We just want to remark that the finite extension of relativistic caustics is of striking importance for phenomenology, as will be clear in the next sections.

TABLE II. Radius (in radians) of the caustics of order k with $2 \leq k \leq 7$, for different values of a.

	a = 0.01	a = 0.05	a = 0.1	a = 0.2
$r_{c,2}$	0.00021	0.0052	0.021	0.082
$r_{c,3}$	0.00056	0.014	0.056	0.22
$r_{c,4}$	0.0009	0.023	0.09	0.36
$r_{c,5}$	0.0013	0.031	0.13	0.5
$r_{c,6}$	0.0016	0.04	0.16	0.64
$r_{c,7}$	0.002	0.05	0.2	0.78

V. GRAVITATIONAL LENSING NEAR CAUSTICS

The description of the caustics is the fundamental step for a full description of gravitational lensing. In this section we will give a complete analytic resolution of the Kerr lens equation for sources close to relativistic caustics.

The starting point is the second-order lens equations, built adding (52) to (46) and (53) to (47). Let us consider a source whose distance from the kth-order caustic is of order a^2 (thus being comparable to the caustic size). Then its position can be expressed in the following way

$$\mu_s = a^2 \delta\mu_s, \tag{61}$$

$$\gamma = \gamma_{\rm cau}^{(1)} + a^2 \delta\gamma, \tag{62}$$

where $\gamma_{\rm cau}^{(1)}$ is the caustic position at the first order in a, expressed by Eq. (51). Correspondingly, the images associated to the critical curve of order k will be enhanced. They will be described by

$$\psi = k\pi + a^2 \delta\psi. \tag{63}$$

Substituting Eqs. (61)–(63) in the lens equations, the zero and first-order terms cancel out and we are only left with the second-order terms

$$\delta\mu_s = S\frac{(-1)^k}{9}\sqrt{1-\xi^2}[9\delta\psi + (1-\xi^2)(5k\pi + 8\sqrt{3} - 20)], \tag{64}$$

$$\delta\gamma = -\frac{\xi}{9}[9\delta\psi - 32 + (3-\xi^2)(5k\pi + 8\sqrt{3} - 20)]. \tag{65}$$

This is the Kerr lens equation close to the caustic of order k. S is just a sign which takes into account the fact that the (ψ, ξ) parametrization only covers half of the observer sky. So, $S = +1$ for the upper half of the observer sky and $S = -1$ for the lower half. We can easily check that the Jacobian (55) is just a^2 times the Jacobian of this lens equation

$$\frac{D}{a^2} = \frac{\partial(\delta\mu_s)}{\partial\xi}\frac{\partial(\delta\gamma)}{\partial(\delta\psi)} - \frac{\partial(\delta\mu_s)}{\partial(\delta\psi)}\frac{\partial(\delta\gamma)}{\partial\xi}. \tag{66}$$

The surprisingly simple form of the lens equation encourages its analytical resolution. The $\delta\gamma$ equation can be easily solved for $\delta\psi$:

$$\delta\psi = -\frac{\delta\gamma}{\xi} + \frac{1}{9}[32 - (3 - \xi^2)(5k\pi + 8\sqrt{3} - 20)]. \tag{67}$$

Plugging this expression into the $\delta\mu_s$ equation, we can write it in the form

$$\delta\mu_s\xi = -S(-1)^k\sqrt{1 - \xi^2}(\delta\gamma + x_c\xi), \tag{68}$$

where $x_c = r_c/a^2$ and r_c is the semiaxis of the caustic as defined by Eq. (60). Squaring both sides we get a fourth-order equation for ξ

$$x_c^2\xi^4 + 2x_c\delta\gamma\xi^3 + (\delta\gamma^2 + \delta\mu_s^2 - x_c^2)\xi^2 - 2x_c\delta\gamma\xi - \delta\gamma^2 = 0. \tag{69}$$

The real solutions of this equation are images for a source in $((\gamma^{(1)}_{\rm cau} + a^2\delta\gamma, a^2\delta\mu_s)$. It is easy to check that we have two images if the source is outside the caustic and four images if it is inside.

Once we have found the solutions of the squared equation, we have to go back to the original Eq. (68). Each root of Eq. (69) satisfies Eq. (68) only with one choice of S. This determines the half-sky where the image appears. It is the upper half if $S = 1$ and the lower half if $S = -1$. Then, we can easily calculate the value of $\delta\psi$ for each image through (67) and then go back to ϵ by Eqs. (32) and (23). Finally we can write the images as

$$D_{OL}\theta_1 = -\frac{3\sqrt{3}}{2}\xi(1 + \epsilon_{cr}) + 2a[1 + \epsilon_{cr}(1 - \xi^2)] + \frac{a^2\xi}{6\sqrt{3}}[12 - 6\xi^2 + \epsilon_{cr}(76 - 82\xi^2 + 27\delta\psi)], \tag{70}$$

$$D_{OL}\theta_2 = S\frac{3\sqrt{3}}{2}\sqrt{1 - \xi^2}\Big[(1 + \epsilon_{cr}) + \frac{4}{3\sqrt{3}}a\xi\epsilon_{cr} + \frac{a^2}{27}(6\xi^2 - \epsilon_{cr}(48 - 82\xi^2 + 27\delta\psi))\Big], \tag{71}$$

with ξ and $\delta\psi$ solving Eqs. (64) and (65).

In the particular case $\delta\mu_s = 0$ (source on the equatorial plane), the solutions are $\xi = \pm 1$ and $\xi = \delta\gamma/x_c$ (double root). The first two solutions are two images staying on the equatorial plane, which are physical for any value of $\delta\gamma$. The other two are acceptable only if $|\delta\gamma| \leq x_c$ because ξ is defined in the range $[-1, 1]$. This is in agreement with the fact that x_c represents the caustic semiaxis. These two images form symmetrically w.r.t. the equatorial plane, grazing the critical curve from the outside. When these additional images are present, the former two are inside the critical curve, while when they are absent the remaining images are one inside and the other outside of the critical curve so that global parity is conserved in caustic crossing.

On the other hand, if $\delta\gamma = 0$, we have the solutions $\xi = 0$ (double root) and $\xi = \pm\sqrt{1 - (\delta\mu_s/x_c)^2}$. The first two form very close to the polar direction on opposite sides of the critical curve, while the last two are real only for $|\delta\mu_s| < x_c$. They form symmetrically w.r.t. the polar direction and graze the critical curve from the inside. As before, things work in such a way that global parity is conserved.

Now let us make an example with a physical source and a physical black hole. Sgr A* has a mass of 3.61×10^5 solar masses. Let us suppose that its spin is $a = 0.02$ (Liu and Melia estimate $a = 0.044$ [32], but different methods point to different values). Then we are able to calculate the caustic positions and shapes. As a source, consider a star with a radius $R_S = 3R_\odot$ at 200 AU from Sgr A*. This is the order of magnitude of the periapse distance of the observed stars orbiting Sgr A*, like S2 or S14 [2]. In Fig. 6 we show what we would see if this star approaches the first retrolensing caustic. The position of this caustic is in $\gamma = 177.98°$, so slightly displaced from the optical axis. This means that the source should be almost in front of the observer, very close to the optical axis. On the left panels of Fig. 6 we show several positions of the source relative to the caustic, as seen by the black hole. Notice that with these values of a, source radius, and distance the size of the source is comparable to that of the caustic. On the right panels, we show the corresponding images and the shadow in dashed style. We see that when the source is far from the caustic (top panels) there are two small images. The bigger one is below the black hole if the source is above the equatorial plane (we recall that this is normal in a retrolensing situation). When the source approaches the caustic (second row panels), the two images do not lie on opposite sides w.r.t the black hole. This distortion is a consequence of the axial symmetry breaking. When the source enters the caustic, two more images form (third and fourth row panels). If the source orbits with a velocity of the order of the circular orbit speed $\sqrt{GM/D_{LS}}$, the whole caustic crossing takes 3.4 hours, much longer than the typical times of the primary caustic crossing, which takes just few seconds [26]. Furthermore, since the higher-order caustics are much more extended, the probability of caustic crossing is much higher.

In Fig. 7 we have shown the case where the same source approaches the first relativistic standard lensing caustic ($k = 3$), which now is displaced to $\gamma = 4.8°$ on the right of the black hole. As this caustic is larger, the source now looks smaller compared to the caustic, as we see in the left panels. When the source is far from the caustic (top panels), there are two images, the bigger one being on the same side of the source (standard lensing situation). As the

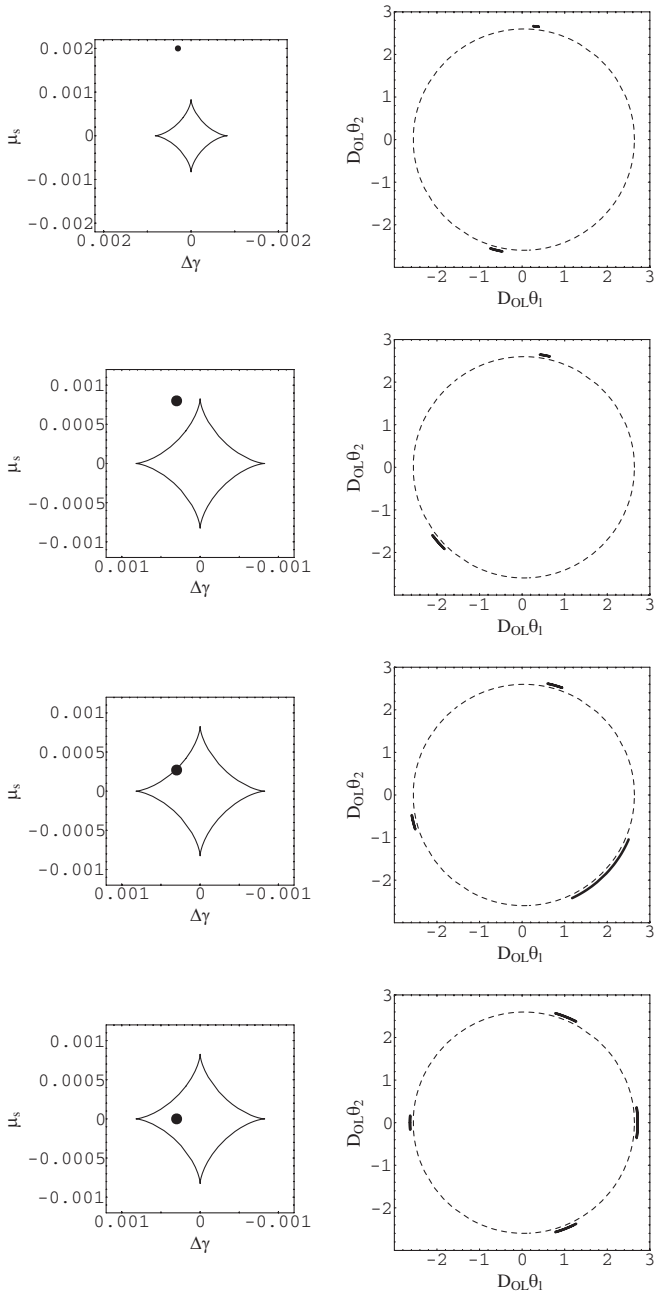

FIG. 6. Formation of the images for a source approaching the first retrolensing caustic ($k = 2$). On the left we show several positions for a source and on the right we have the corresponding images around the shadow (in dashed style). The thickness of the images has been exaggerated to make them more evident.

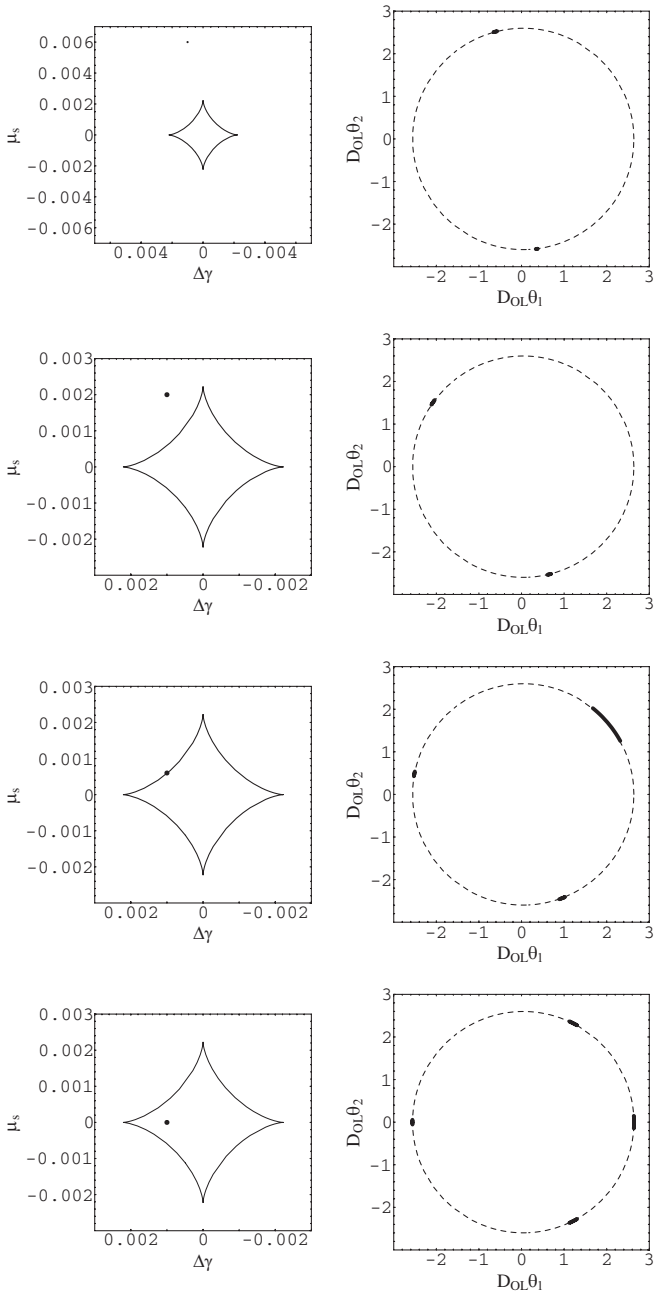

FIG. 7. Formation of the images for a source approaching the first relativistic standard lensing caustic ($k = 3$). On the left we show several positions for a source and on the right we have the corresponding images around the shadow (in dashed style). The thickness of the images has been exaggerated to make them more evident.

source approaches, the images and the black hole are no longer on the same line (second row panels), then formation of two new images takes place (third and fourth row panels). In this case, the caustic crossing takes 9.2 hours, for a source velocity equal to the circular orbit velocity.

Figure 8 zooms on two images generated by different sources in the caustics $k = 2$ and $k = 3$. The first source generates the outer tangential arc while the second source generates the inner tangential arc. This is because the more loops the photons perform, the closer they get to the black hole. Then higher-order images appear closer and closer to the shadow. What is astonishing of this picture is the tremendously small thickness of the arcs. These may be greatly elongated and even form full rings if the source is larger than the caustic, but their radial size is really very

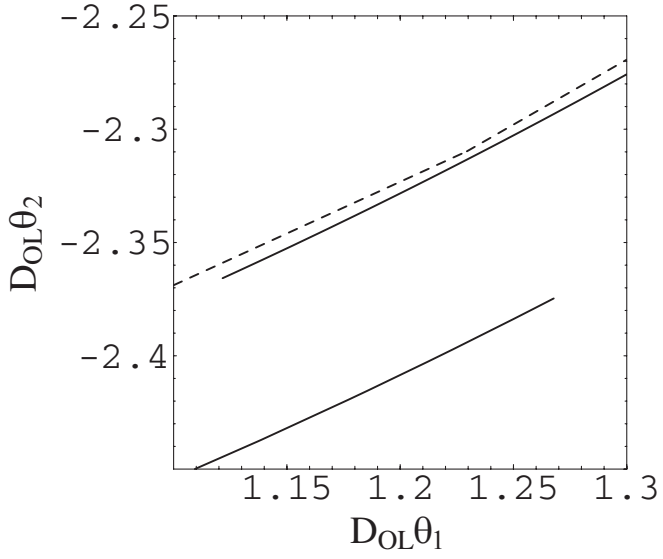

FIG. 8. A zoom very close to the shadow border (in dashed style), showing at the same time the images of two sources, one being in the $k = 2$ caustic (outer tangential arc) and the other being in the $k = 3$ caustic (inner tangential arc).

small. In Figs. 6 and 7, we had to exaggerate the thickness in order to show them in a more evident way. The next section will be devoted to the calculation of the length and the thickness of the arcs, i.e. the magnification of the images.

A. Magnification

In standard weak field gravitational lensing the magnification is the ratio between the angular area of an image and the angular area of the source if no lensing occurred. This does not necessarily make sense when high deflection takes place, since the side of the source seen by the black hole is generally different from the side seen by the observer. Then, if the source does not emit isotropically, a magnification calculated in the standard way would not give the correct ratio between the brightness of the image and that of the source. For example, in the retrolensing situation, the source is in front of the black hole. So the photons going toward the black hole leave the source from the side opposite to the one seen by the observer. For simplicity, in this section we shall assume that the source emits isotropically. The formulae can be easily corrected in the case this does not happen. The isotropic emission hypothesis ensures that the source as seen by the observer is simply D_{LS}^2/D_{OS}^2 smaller than as seen by an observer in the black hole position in the absence of the lens.

The angular area of the image in the observer sky is simply $d\theta_1 d\theta_2$. The angular area of the source in the black hole Boyer-Lindquist coordinates is $|\sin\vartheta_s d\gamma d\vartheta_s| = d\gamma d\mu_s$, when the source is very far from the black hole. Then, the magnification matrix is just the Jacobian matrix of the lens map in the form

$$\begin{cases} \gamma = \gamma(\theta_1, \theta_2) \\ \mu_s = \mu_s(\theta_1, \theta_2) \end{cases}. \tag{72}$$

Yet, we have Eqs. (64) and (65) in the form

$$\begin{cases} \delta\gamma = \delta\gamma(\delta\psi, \xi) \\ \delta\mu_s = \delta\mu_s(\delta\psi, \xi) \end{cases} \tag{73}$$

and Eqs. (70) and (71) in the form

$$\begin{cases} \theta_1 = \theta_1(\delta\psi, \xi) \\ \theta_2 = \theta_2(\delta\psi, \xi) \end{cases}. \tag{74}$$

Then we can find the Jacobian matrix of Eq. (72) as

$$\frac{\partial(\gamma, \mu_s)}{\partial(\theta_1, \theta_2)} = a^2 \frac{\partial(\delta\gamma, \delta\mu_s)}{\partial(\delta\psi, \xi)} \left[\frac{\partial(\theta_1, \theta_2)}{\partial(\delta\psi, \xi)}\right]^{-1}, \tag{75}$$

where we have used the matrix notation

$$\frac{\partial(y_1, y_2)}{\partial(x_1, x_2)} = \begin{pmatrix} \frac{\partial y_1}{\partial x_1} & \frac{\partial y_1}{\partial x_2} \\ \frac{\partial y_2}{\partial x_1} & \frac{\partial y_2}{\partial x_2} \end{pmatrix} \tag{76}$$

and we have noted that $d\gamma = a^2 d(\delta\gamma)$ and $d\mu_s = a^2 d(\delta\mu_s)$.

Then writing the explicit expression of the elements of J is straightforward, once we correctly take care of all the signs. We will not write them here, but we shall give the two eigenvalues of the Jacobian matrix

$$\lambda_r = \frac{2D_{OL}}{3\sqrt{3}\epsilon_{cr}}, \tag{77}$$

$$\lambda_t = \frac{2D_{OL}}{3\sqrt{3}(1 + \epsilon_{cr})} D_0, \tag{78}$$

with D_0 being proportional to the Jacobian studied in the former section (55)

$$\begin{aligned} D_0 &= \pm\sqrt{1 - \xi^2} D \\ &= \frac{(-1)^k a^2}{9}[9\delta\psi - (92 - 24\sqrt{3} - 15k\pi)(1 - \xi^2)]. \end{aligned} \tag{79}$$

Since ϵ_{cr} is fixed by the caustic order k, λ_r is always positive, while λ_t vanishes whenever D_0 does. This condition is fulfilled when Eq. (56) holds, i.e. on critical images. It is possible to show that the two eigenvectors associated to λ_r and λ_t, respectively become radial and tangential in the limit $a \to 0$. So, when the source is close to a caustic, all images are elongated in a direction nearly tangential to the critical curve, as already noticed in the previous subsection. We shall call λ_r and λ_t radial and tangential eigenvalues, respectively, though they are such only in the limit $a \to 0$, actually.

Finally, we can write the radial and tangential magnification of the images w.r.t. the source as seen by the observer. These are

$$\mu_r = \frac{D_{OS}}{D_{LS}} \frac{1}{\lambda_r} = \frac{D_{OS}}{D_{LS}} \frac{3\sqrt{3}\epsilon_{cr}}{2D_{OL}}, \tag{80}$$

$$\mu_t = \frac{D_{OS}}{D_{LS}} \frac{1}{|\lambda_t|} = \frac{D_{OS}}{D_{LS}} \frac{3\sqrt{3}(1+\epsilon_{cr})}{2D_{OL}|D_0|}. \tag{81}$$

Of course, the total magnification is $\mu = \mu_r \mu_t$. A good check is to reduce this formula in the Schwarzschild limit to compare with Refs. [12,14,17,20], and in the equatorial limit, to compare with Ref. [27]. The first limit is obtained sending a to zero keeping the source position ($a^2\delta\gamma$, $a^2\delta\mu_s$) fixed. This is equivalent to put x_c to zero in Eqs. (69) and (67). Then the images are in

$$\xi = \pm\delta\gamma/\sqrt{\delta\gamma^2 + \delta\mu_s^2}, \tag{82}$$

$$\delta\psi = -\frac{16\delta\mu_s^2}{9(\delta\gamma^2 + \delta\mu_s^2)} \mp \sqrt{\delta\gamma^2 + \delta\mu_s^2}. \tag{83}$$

Substituting in Eq. (81), we find

$$\mu_{\rm Sch} = \frac{D_{OS}^2}{D_{LS}^2 D_{OL}^2} \frac{27\epsilon_{cr}(1+\epsilon_{cr})}{4a^2\sqrt{\delta\gamma^2 + \delta\mu_s^2}}. \tag{84}$$

Identifying $a^2\sqrt{\delta\gamma^2 + \delta\mu_s^2}$ with the misalignment of the source with the pointlike caustic position, we exactly find the magnification of Refs. [12,20].

The equatorial limit is recovered when $\delta\mu_s = 0$. Then we have two equatorial images plus two nonequatorial images if the source is inside the caustic. The two equatorial images are described by

$$\xi = \pm 1, \tag{85}$$

$$\delta\psi = -r_c \mp \delta\gamma. \tag{86}$$

Inserting these values in Eq. (81), we find

$$\mu_{eq} = \frac{D_{OS}^2}{D_{LS}^2 D_{OL}^2} \frac{27\epsilon_{cr}(1+\epsilon_{cr})}{4a^2|\delta\gamma \pm r_c|}, \tag{87}$$

which is the leading term close to the equatorial cusps as found in Ref. [27].

The magnification of relativistic images is usually very low. This is expected by the fact that a very small perturbation in the photon trajectory may completely change its final direction. Referring to a source at 100 AU from Sgr A*, by Eq. (80) we find a radial magnification

$$\mu_r^{(2)} = 5.3 \times 10^{-5} \left(\frac{100\ AU}{D_{LS}}\right), \tag{88}$$

$$\mu_r^{(3)} = 2.3 \times 10^{-6} \left(\frac{100\ AU}{D_{LS}}\right) \tag{89}$$

for the relativistic images of order 2 and 3, respectively. These very low values, which are independent (at lowest order) of the distance of the source from the caustic, justify the very thin arcs of Fig. 8.

The tangential magnification diverges when the source crosses a caustic. However, at most the images may merge to form a full Einstein ring, which gives the maximal tangential magnification. Dividing the angular area of a circular corona of radius $3\sqrt{3}(1+\epsilon_{cr})/(2D_{OL})$ and thickness $\mu_r(2R_S)/D_{OS}$ by the angular area of the source $\pi(R_S/D_{OS})^2$, we obtain the maximal total magnification

$$\mu_{\rm max}^{(2)} = \frac{1}{R_S} \frac{D_{OS}^2}{D_{LS}} \frac{27\epsilon_{cr}(1+\epsilon_{cr})}{D_{OL}^2} = 8.7 \times 10^{-3} \left(\frac{R_S}{R_\odot}\right)^{-1} \left(\frac{D_{LS}}{100\ AU}\right)^{-1}, \tag{90}$$

$$\mu_{\rm max}^{(3)} = \frac{1}{R_S} \frac{D_{OS}^2}{D_{LS}} \frac{27\epsilon_{cr}(1+\epsilon_{cr})}{D_{OL}^2} = 3.8 \times 10^{-4} \left(\frac{R_S}{R_\odot}\right)^{-1} \left(\frac{D_{LS}}{100\ AU}\right)^{-1}. \tag{91}$$

In Fig. 9 we show a map of the tangential magnification centered on the first retrolensing caustic (the caustic order is $k = 2$) for $a = 0.02$. To get the total magnification map, it is necessary to multiply the values on this map by the radial magnification (88), which is practically constant in a the neighborhood of the caustic. It is interesting to note that the tangential magnification is greater than one in a large region surrounding the caustic. This means that the cross section for the generation of large relativistic tangential arcs is quite high. This is a very important characteristic of relativistic images that we are going to exploit in the next section when discussing their observability.

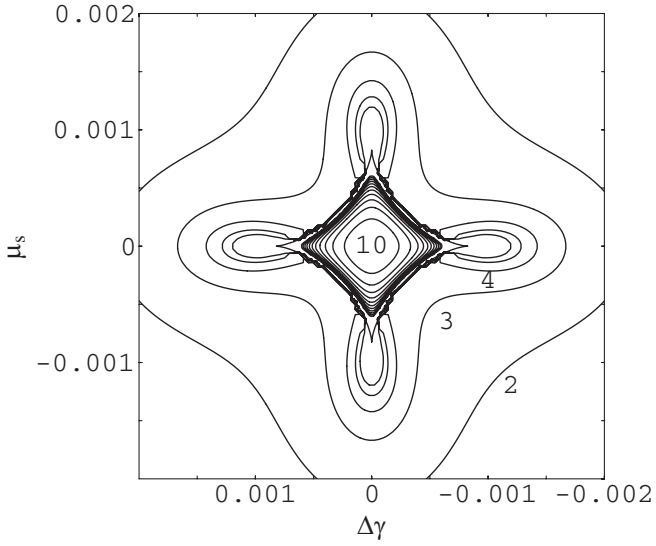

FIG. 9. Tangential magnification map centered on the $k = 2$ caustic (the first retrolensing caustic) for $a = 0.02$ and $D_{LS} = 100\ AU$.

For a source at the center of the caustic, we have an Einstein cross where all images have the same magnification. Then the total magnification takes a very simple expression

$$\mu_c = \frac{D_{OS}^2}{D_{LS}^2 D_{OL}^2} \frac{27\epsilon_{cr}(1+\epsilon_{cr})}{r_c}, \tag{92}$$

where r_c is the semiaxis of the caustic as defined by Eq. (60).

VI. PERSPECTIVES FOR OBSERVATIONS

The relativistic images appear just outside the shadow of the black hole. In order to distinguish them, we need a resolution of the order of μas. The present world record has been achieved with very long baseline interferometry (VLBI) in the mm band and amounts to 18 μas [5]. However, in this band, there are no good compact candidate sources around Sgr A* for gravitational lensing. More interesting are the infrared and especially the x-ray band.

A. Infrared band

In the infrared K-band, centered at $\lambda = 2.2$ μm, the extinction by interstellar dust allows good observations of the stellar environment around Sgr A* [2]. Many stars have been detected and followed during their orbital motion around Sgr A*, providing the best dynamical constraints on its mass distribution. Surprisingly, these stars are of early spectral types, leaving open the question on the presence of such young stars in the galactic center. In the K-band, these stars have magnitudes between $m_K = 13$ and $m_K = 16$.

As regards the angular resolution in the K-band, the VLT units can be combined to perform interferometry observations with an equivalent baseline of 200 m and a maximal angular resolution of 2.2 mas (http://www.eso.org/projects/vlti). Some space missions performing nulling interferometry (TPF, http://www.terrestrial-planet-finder.com; DARWIN, http://ast.star.rl.ac.uk/darwin) should be launched in the near future. According to the mission designs, some spacecraft should fly in formation at distances of the order of tens of meters. A futuristic development of such idea might lead to much higher resolutions. The baseline needed for 1 μas resolution is of the order of hundreds of kilometers. High precision formation flying may be achieved by laser ranging and microthrusters in the wake of what is being studied for LISA (http://lisa.nasa.gov), where the distance between the spacecraft is 5×10^6 km.

Some of the stars around Sgr A* may cross some caustics and generate bright relativistic images. However, they would be embedded in the flux coming from Sgr A* environment. In the quiescent state, Sgr A* flux in the K-band should have $m_K \gtrsim 18.8$ [33]. The infrared emission of Sgr A* is believed to originate in the inner 10 Schwarzschild radii of the black hole [34], with the Schwarzschild radius being

$$R_{\rm Sch} = \frac{2GM}{c^2} = 1.1 \times 10^{10} \text{ m}. \tag{93}$$

Then it is necessary to establish whether relativistic images can overcome the background flux. As conservation of surface brightness holds in gravitational lensing, the relativistic images must have the same surface brightness of the original source as seen by the observer,

$$I_S = \frac{L_S}{4\pi D_{OS}^2 \Omega_S}, \tag{94}$$

where L_S is the intrinsic luminosity of the source, $D_{OS} \simeq 8$ kpc is the distance to the source, and Ω_S is the angular area in the sky subtended by the source, which is $\Omega_S \simeq \pi(R_S)^2/D_{OS}^2$. For a source of 10 solar radii with $m_K = 15$, the surface brightness of the relativistic images is 4 order of magnitudes larger than that of Sgr A*.

However, relativistic images have a tiny angular area and their contribution to the number of photons collected by a pixel in a CCD detector may be very small. To get an idea of this fact, let us consider a CCD detector where every pixel collects energy flux from an angular area of size ω_p^2. If a relativistic image, in the form of a tangential arc of angular thickness $\omega_{\rm arc} = \mu_r(2R_S)/D_{OS}$, lies on the pixel area, the flux received is $S \propto I_S(\omega_p \times \omega_{\rm arc})$. On the other hand, the noise coming from the environment of Sgr A* to the single pixel is $N \propto I_{\rm Sgr}\omega_p^2$. Then, the signal-to-noise ratio for a single pixel is

$$\frac{S}{N} = \frac{I_S}{I_{\rm Sgr}} \frac{\omega_p}{\omega_{\rm arc}} \tag{95}$$

$$\simeq 2.2\left(\frac{\omega_p}{1\ \mu as}\right)^{-1}\left(\frac{R_S}{10\ R_\odot}\right)^{-1}\left(\frac{D_{LS}}{100\ AU}\right)^{-1}, \tag{96}$$

i.e. a pixel with a tangential arc receives only twice more K-band photons than other pixels. The S/N could be improved by taking a smaller pixel size or stars with lower radii and higher brightness, but we cannot go very far. Taking into account absorption by the matter surrounding the black hole that would surely take place and fluctuations in the surface brightness of Sgr A*, we doubt that relativistic images of stellar sources can be actually detected in the K-band by present or near future technology.

B. X-ray band

In the x rays, Chandra is leading very important observations discovering the physics of high energy electromagnetic sources in the central region of the Galaxy [35] with a resolution of the order of 0.5 arcseconds. The space mission project MAXIM (http://maxim.gsfc.nasa.gov) will represent a major leap toward high resolution, reaching the striking resolution of 0.1 μas. With such observational

facility, a complete and detailed imaging of the black hole will be possible.

It is very interesting to consider that Sgr A* luminosity in the 2–10 keV band is 2×10^{33} ergs s^{-1}, which is much lower than expected if the black hole were accreting at the Eddington rate, i.e $L = 3 \times 10^{44}$ ergs s^{-1} [35]. There are several models for Sgr A* accretion. Models based on Bondi accretion (spherically symmetric inflow) predict the x-ray emission to be created in a region of the order of $10^2 R_{\rm Sch}$ [36]. Models based on advection dominated flow [37] predict the emission to be dominated by cooler gas at larger radii, of the order of $10^4 R_{\rm Sch}$.

Indeed, many x-ray sources have been detected in the neighborhood of Sgr A*, with a luminosity comparable or even slightly higher than the supermassive black hole [38]. These sources are probably low mass x-ray binaries (LMXB) which seem very numerous in the galactic center. The situation seems really appealing, since we have a population of bright compact sources, with possibly poor contamination from the intrinsic luminosity of Sgr A*. It is believed that most of the x-ray emission from a LMXB comes from a region of tens of kilometers. Then we can assume $R_S \simeq 10^2$ km, with an x-ray flux of $L_S \simeq L_{\rm Sgr} = 2 \times 10^{33}$ ergs s^{-1}. If we consider an emitting region of $10^2 R_{\rm Sch}$ for Sgr A*, there are 14 orders of magnitude between the surface brightness of a LMXB and the surface brightness of the x-ray emission of the supermassive black hole environment. Then, the signal-to-noise ratio for a single pixel imaging a tangential arc, Eq. (95), is

$$\frac{S}{N} = 0.9 \times 10^6 \left(\frac{\omega_p}{1\ \mu\text{as}}\right)^{-1} \left(\frac{R_S}{100\ \text{km}}\right)^{-1} \left(\frac{D_{LS}}{100\ AU}\right)^{-1}, \tag{97}$$

i.e. the signal in a pixel touched by a tangential arc is nearly 6 order of magnitudes higher than the noise from Sgr A* environment for a detector with the accuracy of 1 μas. The contamination from Sgr A* environment seems to be completely under control. Relativistic gravitational self-lensing of Sgr A* would just produce relativistic Einstein rings with the same surface brightness of Sgr A*. The only serious danger for photons coming from outside Sgr A* and deflected by the central black hole is absorption by the matter surrounding it. However, even if some absorption certainly occurs, it seems difficult to fill a gap of so many orders of magnitudes between the surface brightness of the relativistic images and that of Sgr A* without affecting the luminosity of Sgr A* as well.

Of course, the idea firstly proposed by Rauch and Blandford that some x-ray flares may be explained by lensing of nearby sources is fully plausible in this scenario [26].

VII. CONCLUSIONS

In this paper we have made an analytical treatment of gravitational lensing by Kerr black holes in the strong deflection limit. In order to achieve our objective we have made three approximations.

The first one is the strong deflection limit approximation for all radial integrals. This is just an expansion of the elliptic integrals that result from integrations over the full radial motion of a photon. Restricting to photons suffering a very large deflection, for all the radial integrals we have only kept the leading term diverging as $\log\epsilon$ and the constant term (ϵ being the separation between the image and the shadow border as seen by the observer). As shown in several articles, this limit gives a very good approximation starting from photons deflected by an angle of order π [1,7,12,14].

The second approximation has been to consider only small values of the black hole spin a. This has allowed us to take the Schwarzschild gravitational lensing as a starting point for the derivation of the corrections due to the presence of an intrinsic angular momentum of the black hole. As far as we could compare our results with available exact ones, we have verified a considerably wide applicability range of our approximation. For the first relativistic images, we can safely apply our treatment up to $a = 0.1$ ($a = 0.5$ being the extremal Kerr black hole in our units).

The third restriction concerns the position of source and observer. Besides the limitation to far sources and observers ($D_{LS}, D_{OL} \gg R_{\rm Sch}$), we have also restricted to equatorial observers. This considerably simplifies all calculations without affecting the complete investigation of the most significant physical situation, namely, the black hole in Sgr A*. In fact, it is natural to assume that the equatorial plane of this supermassive black hole coincides with the galactic plane. In any case, a full investigation stepping beyond these restrictions is in progress.

The first achievement of this paper has been the analytical description of the Kerr caustics. At the first order in a we find that they are just shifted along the equatorial plane still remaining pointlike, while at second order they are resolved into typical diamond-shaped figures. We are thus able to calculate the position and the extension of the caustics for any order of relativistic images (as long as we remain in the perturbative regime). As stated in Section IV, the strong deflection limit treatment does not cover the primary caustic ($k = 1$ in our formulae), since this caustic is formed in the weak field regime for $D_{LS} \gg 1$ [26,39]. With no regard to the lensing regime, the effect of the angular momentum of the deflector is similar, with caustics getting a diamond-shaped structure and drifting from the optical axis. Whereas magnification effects due to the primary caustic are very large, its size is very small, so that the creation of additional pairs of images (which is the most evident manifestation of the presence of a non-negligible spin) is very difficult to achieve. The significant extension of relativistic caustics strongly enhances the cross section for additional images and puts them in a much better position for testing the Kerr nature of the black

hole. It has to be remarked that our perturbative investigation still leaves open the possibility that metamorphosis may occur at large values of a. Though this has been numerically excluded for the primary caustic [26], it is possible that higher-order caustics develop more complicated structures in a strongly nonpertubative regime.

The second achievement has been the analytical inversion of the lens mapping near the caustics, which has allowed us to draw fascinating pictures of the relativistic images generated by a hypothetical source close to a relativistic caustic.

However, the most important result has been the possibility of doing concrete analytical estimates of the size and luminosity of the relativistic images. The LMXBs surrounding Sgr A* provide an ideal population of sources, which may eventually bump into a relativistic caustic and generate appreciable relativistic images. This is because they are compact sources with very high surface brightness in the x rays, compared to that of Sgr A*. This seems not to be the case for stellar sources in the infrared K-band, which have too little surface brightness. Using our formulae for the magnification of relativistic images, we are entitled to claim that future space missions performing x-ray interferometry with resolutions of the order of 1 μas will see these relativistic images with high probability.

ACKNOWLEDGMENTS

V. B. and M. S. thank all the participants of the workshop ''Gravitational Lensing in the Kerr Spacetime Geometry,'' held at the American Institute of Mathematics in Palo Alto (CA), for invaluable discussions and precious interaction, and, in particular, Simonetta Frittelli and Arlie Petters for the kind invitation. V. B. and G. S. acknowledge support for this work by MIUR through PRIN 2004 ''Astroparticle Physics'' and by research fund of the Salerno University. F. D. L.'s work was performed under the auspices of the EU, which has provided financial support to the ''Dottorato i Ricerca Internazionale in Fisica della Gravitazione ed Astrofisica'' of the Salerno University, through ''Fondo Sociale Europeo, Misura III.4.''

APPENDIX A: RESOLUTION OF RADIAL INTEGRALS

In this appendix we recall the SDL technique used in Ref. [17] to solve radial integrals, applying it to the integrals that appear in the geodesics equations. We rewrite them here for an easier reading

$$I_1 = 2\int_{x_0}^{\infty} \frac{dx}{\sqrt{R}}, \tag{A1}$$

$$I_2 = 2\int_{x_0}^{\infty} \frac{x^2 + a^2 - aJ}{\Delta\sqrt{R}}\, dx. \tag{A2}$$

First we change the integration variable from x to z by the transformation

$$x = \frac{x_0}{1 - z}. \tag{A3}$$

As a consequence, the integration domain $[x_0, \infty]$ becomes $[0, 1]$.

Then, each of the integrals I_1, I_2 can be written in the form

$$I_i = \int_0^1 R_i(z) f(z) dz, \tag{A4}$$

$$f(z) = \frac{1}{\sqrt{R(z)}}, \tag{A5}$$

where the two functions $R_i(z)$ can be easily read by Eqs. (24) and (25) taking into account the Jacobian of the transformation (A3):

$$R_1(z) = \frac{2x_0}{(1 - z)^2}, \tag{A6}$$

$$R_2(z) = \frac{2x_0}{(1 - z)^2} \frac{x_0^2 + (1 - z)^2(a^2 - aJ)}{x_0^2 - x_0(1 - z) + a^2(1 - z)^2}. \tag{A7}$$

Now we consider the expansion of $R(z)$ in a neighborhood of $z = 0$. Since $z = 0$ means $x = x_0$ and x_0 is a root of $R(x)$, we deduce that $R(z = 0) = 0$. Then the expansion of $R(z)$ reads

$$R(z) = \alpha z + \beta z^2 + o(z^2), \tag{A8}$$

where the coefficients of the expansion are

$$\alpha = x_0[(a - J)^2 + Q + 2(a^2 - J^2 - Q)x_0 + 4x_0^3], \tag{A9}$$

$$\beta = x_0[(a - J)^2 + Q + 3(a^2 - J^2 - Q)x_0 + 10x_0^3]. \tag{A10}$$

We use this expansion to define

$$f_0(z) = \frac{1}{\sqrt{\alpha z + \beta z^2}}. \tag{A11}$$

The radial integrals can be split in two pieces

$$I_i = I_{i,D} + I_{i,R}, \tag{A12}$$

$$I_{i,D} = \int_0^1 R_i(0) f_0(z) dz, \tag{A13}$$

$$I_{i,R} = \int_0^1 [R_i(z) f(z) - R_i(0) f_0(z)] dz. \tag{A14}$$

The first integral gives the result

$$I_{i,D} = \frac{2R_i(0)}{\sqrt{\beta}} \log\frac{\sqrt{\beta} + \sqrt{\alpha + \beta}}{\sqrt{\alpha}}. \tag{A15}$$

α, β, and $R_i(0)$ are known functions of x_0, J, Q, and a.

Now we can use the SDL parametrizations (20)–(22) for all these quantities, so that they become functions of ξ, δ (or equivalently ϵ), and a. Then, in the spirit of SDL approximation, we keep the leading order in δ, which goes as $\log\delta$, and the next-to-leading order which is constant in δ. Finally, we expand the obtained expression to second order in a.

As regards the integrals $I_{i,R}$, the integrand function is regular in the whole integration domain. Sending δ to zero, the integrand does not diverge. So, this integral contributes to the SDL expansion with another constant in δ plus higher-order terms that we can neglect. It is convenient to make the second-order expansion in a before the integration, in order to have a sum of easily integrable functions. We can then add the result of the integral $I_{i,R}$ to the integral $I_{i,D}$, to reconstruct the full SDL formulae for radial integrals:

$$I_1 = -a_1 \log\delta + b_1, \tag{A16}$$

$$I_2 = -a_2 \log\delta + b_2. \tag{A17}$$

The coefficients expanded to second order in a read

$$a_1 = \frac{4}{3\sqrt{3}} + \frac{16}{27} a\xi + \frac{8}{27\sqrt{3}}(1 + 3\xi^2)a^2, \tag{A18}$$

$$b_1 = a_1 \log[6(\sqrt{3} - 1)^2] - \frac{8}{27\sqrt{3}} a^2(5 - 2\sqrt{3})(1 - \xi^2), \tag{A19}$$

$$a_2 = \frac{4}{\sqrt{3}} + \frac{8}{3} a\xi + \frac{8\sqrt{3}}{27}(1 + 7\xi^2)a^2, \tag{A20}$$

$$\begin{aligned} b_2 = {} & [a_2 + 4(1 + 2a^2)]\log[6(\sqrt{3} - 1)^2] \\ & - 2(1 + 2a^2)\log 48 - \frac{8}{3\sqrt{3}} a\xi(3\sqrt{3} - 2) \\ & + \frac{8}{27} a^2[19\sqrt{3} - 12 + \xi^2(14 - 25\sqrt{3})]. \end{aligned} \tag{A21}$$

The separation of I_i into $I_{i,D}$ and $I_{i,R}$ is necessary to isolate the term generating the $\log\delta$ into an easier integral.

APPENDIX B: ANGULAR INTEGRALS

This appendix is devoted to the resolution of the angular integrals

$$J_1 = \pm \int \frac{1}{\sqrt{\Theta}} d\vartheta, \tag{B1}$$

$$J_2 = \pm \int \frac{csc^2\vartheta}{\sqrt{\Theta}} d\vartheta. \tag{B2}$$

Introducing the variable $\mu = \cos\vartheta$, the two integrals become

$$J_1 = \pm \int \frac{1}{\sqrt{\Theta_\mu}} d\mu, \tag{B3}$$

$$J_2 = \pm \int \frac{1}{(1 - \mu^2)\sqrt{\Theta_\mu}} d\mu, \tag{B4}$$

where

$$\Theta_\mu = a^2(\mu_-^2 + \mu^2)(\mu_+^2 - \mu^2), \tag{B5}$$

$$\mu_\pm^2 = \frac{\sqrt{b_{JQ}^2 + 4a^2 Q_m} \pm b_{JQ}}{2a^2}, \tag{B6}$$

$$b_{JQ} = a^2 - J_m^2 - Q_m, \tag{B7}$$

and we have already replaced J and Q with J_m and Q_m, coherently with the fact that we only retain terms which are logarithmically diverging or constant in δ (or equivalently ϵ).

Θ_μ has two zeros in $\mu = \pm\mu_+$. Then the photon performs symmetric oscillations of amplitude μ_+ w.r.t. the equatorial plane. It is useful to write the explicit expressions of μ_+ and μ_- in terms of a and ξ, using Eqs. (12) and (13) and expanding to second order in a. We find

$$\mu_+ = \sqrt{1 - \xi^2}\left(1 + \frac{4a\xi}{3\sqrt{3}} - \frac{8a^2\xi^2}{27}\right), \tag{B8}$$

$$\mu_- = \frac{3\sqrt{3}}{2a} - 2\xi + \frac{a(4 - 8\xi^2)}{3\sqrt{3}} + \frac{4a^2\xi(12 - 17\xi^2)}{27}. \tag{B9}$$

The oscillation amplitude is $\sqrt{1 - \xi^2}$ plus corrections due to the black hole spin. This is coherent with the fact that for a photon reaching the observer from the equatorial plane ($\xi = \pm 1$) the amplitude of the oscillation goes to zero. On the other hand, a photon moving on a polar orbit ($\xi = 0$) performs oscillations of maximal amplitude, touching the poles of the black hole. Now, to perform the angular integrals, it is wise to expand the integrands to second order in a and then integrate. Then, the primitive functions read

$$F_{J_1}(\mu) = \frac{2}{3\sqrt{3}} \arcsin\frac{\mu}{\sqrt{1-\xi^2}} + \frac{8}{27} a\xi\left[\arcsin\frac{\mu}{\sqrt{1-\xi^2}} - \frac{\mu}{\sqrt{1-\mu^2-\xi^2}}\right] + \frac{2a^2}{81\sqrt{3}}\left[(33\xi^2-9)\arcsin\frac{\mu}{\sqrt{1-\xi^2}} + \frac{\mu(\mu^4+2\mu^2(\xi^2-1)+1+6\xi^2-7\xi^4)}{(1-\mu^2-\xi^2)^{3/2}}\right], \tag{B10}$$

$$F_{J_2}(\mu) = \frac{2}{3\sqrt{3}\xi} \arctan\frac{\mu\xi}{\sqrt{1-\mu^2-\xi^2}} + \frac{8}{27\xi^2} a\left[\arctan\frac{\mu\xi}{\sqrt{1-\mu^2-\xi^2}} - \frac{\mu\xi}{\sqrt{1-\mu^2-\xi^2}}\right] + \frac{4a^2}{81\sqrt{3}}\left[\frac{12-21\xi^2+20\xi^4}{\xi^3}\arctan\frac{\mu\xi}{\sqrt{1-\mu^2-\xi^2}} + \frac{4\mu(1-\xi^2)(3\mu^2-3+4\xi^2)}{\xi^2(1-\mu^2-\xi^2)^{3/2}} + \arctan\frac{\mu}{\sqrt{1-\mu^2-\xi^2}}\right]. \tag{B11}$$

The integration limits are the values of μ at the observer and source position. The observer is at $\mu_o = 0$, since it lies on the equatorial plane, while the source is in $\mu_s = \cos\vartheta_s$. Notice that the choice of an equatorial observer leads to a considerable simplification, since $F_{J_1}(0) = F_{J_2}(0) = 0$. Moreover, we have to consider that during the photon motion, μ may perform several oscillations between $-\mu_+$ and μ_+, depending on how many loops the photon makes around the black hole before escaping. So, we have to add an arbitrary integer number m of integrals covering the whole domain $[-\mu_+, \mu_+]$. The final results read

$$J_1 = \pm F_{J_1}(\mu_s) + \frac{2m\pi}{3\sqrt{3}}\left[1 + \frac{4a\xi}{3\sqrt{3}} + \frac{a^2(11\xi^2-3)}{9}\right], \tag{B12}$$

$$J_2 = \pm F_{J_2}(\mu_s) + \frac{2m\pi}{3\sqrt{3}\xi}\left[1 + \frac{4a}{3\sqrt{3}\xi} + \frac{2a^2(12-21\xi^2+\xi^3+20\xi^4)}{27\xi^2}\right], \tag{B13}$$

where the minus signs hold if the photon initially increases its latitude and the plus signs hold if the latitude decreases initially.

[1] C. Darwin, Proc. R. Soc. A **249**, 180 (1959).
[2] F. Eisenhauer, R. Genzel, T. Alexander *et al.*, Astrophys. J. **628**, 246 (2005).
[3] F. Melia and H. Falcke, Annu. Rev. Astron. Astrophys. **39**, 309 (2001).
[4] K. S. Virbhadra and G. F. R. Ellis, Phys. Rev. D **62**, 084003 (2000).
[5] T. P. Krichbaum *et al.*, in Proceedings of the 6th European VLBI Network Symposium, Bonn, Germany, edited by E. Ros, R. W. Porcas, A. P. Lobanov, and J. A. Zensus (unpublished).
[6] H. Falcke, F. Melia, and E. Agol, Astrophys. J. **528**, L13 (2000).
[7] V. Bozza and L. Mancini, Astrophys. J. **627**, 790 (2005).
[8] S. Frittelli and E. T. Newman, Phys. Rev. D **59**, 124001 (1999); S. Frittelli, T. P. Kling, and E. T. Newman, Phys. Rev. D **61**, 064021 (2000); M. P. Dabrowski and F. E. Schunck, Astrophys. J. **535**, 316 (2000); K. S. Virbhadra and G. F. R. Ellis, Phys. Rev. D **65**, 103004 (2002).
[9] V. Perlick, Phys. Rev. D **69**, 064017 (2004).
[10] R. D. Atkinson, Astron. J. **70**, 517 (1965).
[11] J. P. Luminet, Astron. Astrophys. **75**, 228 (1979).
[12] H. C. Ohanian, Am. J. Phys. **55**, 428 (1987).
[13] R. J. Nemiroff, Am. J. Phys. **61**, 619 (1993).
[14] V. Bozza, S. Capozziello, G. Iovane, and G. Scarpetta, Gen. Relativ. Gravit. **33**, 1535 (2001).
[15] E. F. Eiroa, G. E. Romero, and D. F. Torres, Phys. Rev. D **66**, 024010 (2002).
[16] A. O. Petters, Mon. Not. R. Astron. Soc. **338**, 457 (2003).
[17] V. Bozza, Phys. Rev. D **66**, 103001 (2002).
[18] A. Bhadra, Phys. Rev. D **67**, 103009 (2003); E. F. Eiroa, Phys. Rev. D **71**, 083010 (2005); R. Whisker, Phys. Rev. D **71**, 064004 (2005); A. S. Majumdar and N. Mukherjee, Int. J. Mod. Phys. D **14**, 1095 (2005); J. M. Tejeiro and E. A. Larranaga, gr-qc/0505054.
[19] E. F. Eiroa and D. F. Torres, Phys. Rev. D **69**, 063004 (2004).
[20] V. Bozza and L. Mancini, Astrophys. J. **611**, 1045 (2004).
[21] V. Bozza and L. Mancini, Gen. Relativ. Gravit. **36**, 435 (2004).
[22] B. Carter, Phys. Rev. **174**, 1559 (1968).
[23] S. Chandrasekhar, *Mathematical Theory of Black Holes* (Clarendon, Oxford, 1983).
[24] C. T. Cunningham and J. M. Bardeen, Astrophys. J. **183**, 237 (1973).

[25] S. U. Viergutz, Astron. Astrophys. **272**, 355 (1993); A. de Vries, Classical Quantum Gravity **17**, 123 (2000); R. Takahashi, Astrophys. J. **611**, 996 (2004); K. Beckwith and C. Done, Mon. Not. R. Astron. Soc. **359**, 1217 (2005).
[26] K. P. Rauch and R. D. Blandford, Astrophys. J., **421**, 46 (1994).
[27] V. Bozza, Phys. Rev. D **67**, 103006 (2003).
[28] S. E. Vazquez and E. P. Esteban, Nuovo Cimento Soc. Ital. Fis. B **119**, 489 (2004).
[29] R. H. Boyer and R. W. Lindquist, J. Math. Phys. (Cambridge, Mass.) **8**, 265 (1967).
[30] A. F. Zakharov, A. A. Nucita, F. De Paolis, and G. Ingrosso, astro-ph/0411511.
[31] M. J. Reid, Annu. Rev. Astron. Astrophys. **31**, 345 (1993).
[32] S. Liu and F. Melia, Astrophys. J. **573**, L23 (2002).
[33] A. M. Ghez *et al.*, Astrophys. J. **601**, L159 (2004); R. Genzel *et al.*, Nature (London) **425**, 934 (2003).
[34] F. Yuan, E. Quataert, and R. Narayan, Astrophys. J. **606**, 894 (2004).
[35] F. K. Baganoff *et al.*, Astrophys. J. **591**, 891 (2003).
[36] F. Melia, Astrophys. J. **387**, L25 (1992); **426**, 577 (1994).
[37] S. Ichimaru, Astrophys. J. **214**, 840 (1977); M. J. Rees, M. C. Begelman, R. D. Blandford, and E. S. Phinney, Nature (London) **295**, 17 (1982); R. Narayan, I. Yi, and R. Mahadevan, Nature (London) **374**, 623 (1995); M. A. Abramovicz, X. Chen, S. Kato, J.-P. Lasota, and O. Regev, Astrophys. J. **438**, L37 (1995); R. Mahadevan, Nature (London) **394**, 651 (1998).
[38] M. P. Muno *et al.*, Astrophys. J. **622**, L113 (2005).
[39] M. Sereno, Mon. Not. R. Astron. Soc. **344**, 942 (2003).